Photoluminescence Decomposition Analysis: A Technique to Characterize N-V Creation in Diamond

Scott T. Alsid,[1,2] John F. Barry,[1] Linh M. Pham,[1,*] Jennifer M. Schloss,[3,4] Michael F. O'Keeffe,[1] Paola Cappellaro,[2] and Danielle A. Braje[1]

[1] *Lincoln Laboratory, Massachusetts Institute of Technology, Lexington, Massachusetts 02421, USA*
[2] *Department of Nuclear Science and Engineering, Massachusetts Institute of Technology, Cambridge, Massachusetts 02139, USA*
[3] *Department of Physics, Massachusetts Institute of Technology, Cambridge, Massachusetts 02139, USA*
[4] *Center for Brain Science, Harvard University, Cambridge, Massachusetts 02138, USA*

(Received 19 March 2019; revised manuscript received 26 June 2019; published 1 October 2019)

Treatment of laboratory-grown diamond by electron irradiation and annealing has enabled quantum sensors based on negatively charged nitrogen-vacancy (N-V^-) centers to demonstrate record sensitivities. Here we investigate the irradiation and annealing process applied to 28 diamond samples using an ambient-temperature, all-optical approach. As the presence of the neutrally charged nitrogen-vacancy (N-V^0) center is deleterious to sensor performance, this photoluminescence decomposition analysis is first used to determine the concentration ratio of N-V^- to N-V^0 in diamond samples from the measured photoluminescence spectrum. The analysis hinges on (i) isolating each N-V charge state's emission spectrum and (ii) measuring the N-V^- to N-V^0 emission ratio, which is found to be 2.5 ± 0.5 under low-intensity 532-nm illumination. Using the photoluminescence-decomposition-analysis method, we measure the effects of irradiation and annealing on conversion of substitutional nitrogen to N-V centers. Combining these measurements with a phenomenological model for diamond irradiation and annealing, we extract an estimated monovacancy creation rate of 0.52 ± 0.26 cm^{-1} for 1-MeV electron irradiation and an estimated monovacancy diffusion coefficient of 1.8 nm^2/s at 850 °C. Finally, we find that irradiation doses of 10^{18} e^-/cm^2 or more deteriorate the N-V^- decoherence time T_2, whereas T_1 is unaffected up to the the maximum investigated dose of 5×10^{18} e^-/cm^2.

DOI: 10.1103/PhysRevApplied.12.044003

I. INTRODUCTION

The negatively charged nitrogen-vacancy (N-V^-) center, with its rich spin dynamics even at room temperature, has captured the interest of the sensor community. Importantly, quantum sensors based on N-V^- ensembles in diamond require efficient conversion of substitutional nitrogen to N-V^- centers to achieve peak performance [1–3]. One common approach to creating N-V^--rich diamond material involves electron-irradiating and subsequently annealing nitrogen-doped diamond [2,4–6]. However, maximizing the N-V^- population while minimizing unwanted defects [e.g., neutral N-V (N-V^0) centers, vacancy complexes, and other paramagnetic impurities] is critically dependent on the use of proper irradiation and annealing processes.

Although high-quality diamond-processing studies are available [7] to guide postgrowth treatment, literature discrepancies (see Appendix D 1 and Refs. [8,9]) and a shortage of systematic studies impede full understanding of how these postgrowth treatments affect defect composition. In particular, variation in the base diamond material investigated in the literature studies constitutes a prominent and continuing obstacle to optimizing treatment parameters. For example, diamond origin (natural or synthetic), growth method [chemical vapor deposition (CVD) or high pressure and high temperature (HPHT)], nitrogen concentration [10–12], lattice defect density, impurity concentration [13], and strain [13] have all been shown to affect the irradiation and annealing process. As diamond-synthesis capabilities develop and material is produced with a range of compositions, a comprehensive study of irradiation and annealing will enable targeted diamond engineering for diverse quantum-sensing applications [2,14,15].

To fine-tune the diamond-treatment process, accurate measurements of the effects of irradiation and annealing on key diamond material properties are needed. In particular, optimizing N-V-diamond quantum sensors necessitates post-treatment characterization of (i) the

*linh.pham@ll.mit.edu

conversion efficiency from nitrogen to N-V centers, (ii) the N-V^--to-N-V^0 charge-state ratio, and (iii) the relevant N-V^- spin relaxation times. Such measurements can also provide physical insight into the vacancy creation and diffusion dynamics central to formation of N-V^- centers. Here we present an all-optical, ambient-temperature technique for rapidly characterizing the N-V^--to-N-V^0 charge-state ratio and total N-V concentration. This technique provides an appealing alternative to slower conventional methods, such as electron-paramagnetic-resonance (EPR) and ultraviolet-visible (UV-vis) spectroscopy. Further, the technique is suitable for analyzing N-V-doped layers or other small ensembles, regimes typically precluded from EPR or UV-vis analysis by signal-to-noise requirements. Additionally, accurate charge-state-ratio measurements hinge on knowledge of the photoluminescence (PL) rate of N-V^- relative to N-V^0 for equal concentrations. Here we determine this PL ratio under low-intensity 532-nm excitation.

We demonstrate the presented technique's utility in a systematic study of irradiation and annealing on 28 diamonds. We focus on a diamond base material that is commercially available and relevant to many quantum-sensing applications [2,15]. To support additional analysis of our measurements, we introduce a phenomenological model for the irradiation and annealing process and extract an estimated irradiation-induced vacancy creation rate of 0.52 ± 0.26 cm^{-1} for 1-MeV electron irradiation. From the model, we also determine an estimated monovacancy diffusion coefficient of 1.8 nm^2/s at 850 °C. Further, we examine the effects of irradiation and annealing on the N-V^- coherence time T_2 and longitudinal relaxation time T_1 in the base material investigated. Finally, we comment on applications of the methods and analysis detailed in this work to furthering N-V physics research and diamond materials science. Example near-term studies include characterization of N-V^0 optical dynamics and investigation of the effects of base-material variation on vacancy migration.

II. DIAMOND-MATERIAL OPTIMIZATION

The presence of various electronic spin species in diamond [e.g., N-V^-, N-V^0, substitutional nitrogen (N_S), and other paramagnetic impurities] can limit the achievable sensitivity of a N-V-diamond quantum sensor; this effect motivates the careful engineering of diamond material to contain optimal concentrations of each of these spin defects. In particular, spin-defect concentrations affect three key parameters that can limit sensitivity: measurement time, measurement contrast, and number of photons collected per measurement. For example, measurement time is limited by the dephasing, coherence, or relaxation times of the N-V^- spins, which in turn are typically limited by other spin species generating magnetic noise in the vicinity of the sensing N-V^- centers. Measurement contrast can be degraded by the presence of non-information-containing background-fluorescence emitters such as N-V^0. The number of photons collected per measurement is dictated by the optical collection efficiency of the experimental apparatus and ultimately by the number of N-V centers probed during the measurement.

In essence, the sensitivity of a N-V-diamond quantum sensor can generally be enhanced by maximizing the number of N-V^- centers while minimizing the presence of all other spin defects. Since nitrogen is an integral constituent of the N-V^- center, nitrogen-containing defects often dominate in diamond material used for N-V-ensemble-based sensors. Thus, optimal values of the N-V conversion efficiency $\chi \equiv [\text{N-}V^T]/[\text{N}^T]$ are desired to achieve optimal sensitivity in these devices. Here $[\text{N-}V^T]$ indicates the total N-V population, summed over all charge states, and $[\text{N}^T]$ denotes the total nitrogen concentration in all forms including all charge states (e.g., N_S^0, N_S^+, N-V^0, N-V^-).

There is an important distinction between the N-V^- centers, which are the fundamental sensing qubits that together constitute the N-V-diamond quantum sensor, and N-V^0 centers. The presence of N-V^0 centers degrades sensor performance by several mechanisms. First, the photoluminescence from N-V^0 spectrally overlaps with that of N-V^-, contributing background signal and thereby reducing measurement contrast. This effect is particularly deleterious when N-V^0 concentration is similar to or greater than the N-V^- concentration [16]. Additionally, the N-V^0 center's electronic $S = \frac{1}{2}$ paramagnetic ground state [17] may increase magnetic noise in the diamond and thereby degrade N-V^- spin-coherence times. For these reasons, maximization of the charge-state efficiency $\zeta \equiv [\text{N-}V^-]/[\text{N-}V^T]$ is also desirable.

A simple model suggests N-V^- formation requires two nitrogen atoms and a vacancy. One nitrogen atom captures the vacancy to form the N-V center, while the other nitrogen donates a valence electron to negatively charge the N-V center [18]. For typical CVD diamonds, such as those used in this work, the native grown-in vacancy concentration is too low to achieve optimal N^T-to-N-V^T conversion efficiency $\chi \sim 1/2$. One straightforward approach to increase χ in these diamonds is to use electron irradiation to create vacancies in the crystal lattice. A subsequent annealing step mobilizes the vacancies and enables their capture by N_S defects to form N-V centers. Achieving the optimal spin-defect composition in the diamond following this two-step process is critically dependent on optimizing irradiation and annealing parameters. For example, too low an irradiation dose will introduce too few vacancies relative to N_S defects, limiting the attainable postanneal N-V conversion efficiency χ, which in turn limits the number of N-V^- sensors available to perform measurements. Furthermore, the remaining underutilized paramagnetic N_S defects can degrade N-V^- spin-coherence times. On the other hand, too high an irradiation dose will introduce too

many vacancies relative to N_S, resulting in overproduction of undesirable N-V^0 centers [19] and thereby degrading the charge-state efficiency ζ.

Proper selection of irradiation energy and dose, annealing time and temperature, and other processing parameters is imperative to obtain N-V-diamond optimized for high-sensitivity quantum sensing. Consequently, quantitative characterization of key material properties, such as the N-V^--to-N-V^0 charge-state ratio, is likewise important in determining these optimal processing parameters. Conventional techniques for quantitatively characterizing relevant spin-defect concentrations include UV-vis spectroscopy, which measures N-V^0 and N-V^- concentrations, and EPR spectroscopy, which measures N-V^- and N_S concentrations. Unfortunately, UV-vis spectroscopy is performed at cryogenic temperatures and thus requires additional time for thermal cycling. EPR spectroscopy of typically small diamond volume likewise requires significant averaging time. Since both of these conventional techniques typically take approximately 1 h or longer to perform measurements on a single sample, characterizing the large number (approximately ten or more) of samples typically involved in optimizing processing parameters can be quite onerous. Furthermore, both techniques require specialized equipment, which is not readily accessible in many N-V-diamond research laboratories.

III. EXPERIMENTAL DESIGN

This study uses 28 commercially available diamonds (Element Six, 145-500-0274-01) grown by CVD. The chip-sized samples are $2.6 \times 2.6 \times 0.3$ mm^3, with $\langle 100 \rangle$ edges and {100} face orientations. The diamond material contains carbon in natural isotopic abundance (1.1% ^{13}C, 98.9% ^{12}C) and exhibits a mean total nitrogen concentration of approximately 118 ppb (see Appendix A 1). Before irradiation, the samples are preannealed at 850 °C for 1 h in a 760-Torr nitrogen atmosphere.

Diamond irradiation is performed at a commercial facility (Prism Gem LLC) by a 1-MeV electron beam with a 1-cm nominal diameter. Diamonds are placed on a water-cooled plate maintained at 66 °C or below; the diamonds are estimated to remain below 120 °C during irradiation, suggesting that interstitial-vacancy recombination during irradiation can be ignored [20]. Twenty-five diamonds receive doses systematically varied between 1×10^{15} and 5×10^{19} e^-/cm^2; the other three diamonds remain unirradiated and are retained as controls. Nineteen of the irradiated diamonds are subsequently annealed at 850 °C in a 760-Torr nitrogen atmosphere for 1 h at the same commercial facility. The other six irradiated diamonds and a subset of the 850 °C annealed diamonds are then annealed at 1250 °C under 100-Torr hydrogen gas for 1 h. Each diamond's specific irradiation and annealing parameters are given in Appendix A 2.

Diamond characterization is performed on N-V ensembles with use of a custom-built confocal microscope with an attached spectrometer (see Appendix B 1). While this confocal microscope follows standard designs [21] in most ways, a notable modification allows enhanced functionality for N-V-ensemble excitation power and intensity studies. Specifically, the microscope uses a detection volume centered within a much larger excitation volume, ensuring all N-V centers within the detection volume receive similar optical illumination intensity (see Appendix B 3, Fig. 9). Without this modification, the intensity gradient associated with the wings of a Gaussian excitation profile can complicate interpretation of intensity-induced dynamics, such as photoionization and charge conversion.

A spectrometer attached to the confocal microscope allows spectral characterization of the PL light from 560 to 818 nm. This range allows collection of nearly all emitted PL light from N-V^- and N-V^0 centers; analysis of PL data in the literature from other groups [22–31] suggests this wavelength range covers approximately 99% or more of N-V^- and N-V^0 photoluminescence.

IV. CHARGE-STATE-PHOTOLUMINESCENCE STUDY

In this section, we present our method for quantitatively determining the charge-state efficiency ζ using PL spectroscopy. Historically, approximations of ζ have been extracted from PL spectra [1] using the Debye-Waller factor $\tilde{S}$ [32,33] (see Appendix C 2). However, this method is nonideal because it results in large uncertainties in the extracted ζ and does not account for the difference in PL rate of the different charge states. We use an alternative method for isolating the PL contributions due to N-V^- and N-V^0 for a given PL spectrum. We then use this alternative decomposition method to determine the ratio of PL light produced by a single N-V^- to that produced by a single N-V^0 per unit time. The charge-state photoluminescence ratio of N-V^- relative to N-V^0 is denoted κ_λ for optical excitation at wavelength λ (in this work $\lambda = 532$ nm) For laser intensities where N-V saturation effects can be ignored, the concentration of each charge state is then proportional to its respective PL when corrections are made for κ_{532}. Therefore, the charge-state efficiency may be rewritten as

$$\zeta \equiv \frac{[\text{N-}V^-]}{[\text{N-}V^T]} = \frac{[\text{N-}V^-]}{[\text{N-}V^-] + [\text{N-}V^0]} = \frac{c_-}{c_- + \kappa_{532} c_0}, \quad (1)$$

where c_- and c_0 denote the fractional contributions to total PL from N-V^- and N-V^0, respectively. In the absence of PL from defects besides N-V^0 and N-V^-, $c_- + c_0 = 1$. Postanalysis of our data shows little if any PL contributions in the 550–818-nm range from defects other than

N-V^- and N-V^0 for irradiation doses of approximately 1×10^{19} e^-/cm^2 or less.

A. Photoluminescence-spectrum decomposition

To determine the charge-state efficiency ζ using Eq. (1), the fractional contributions of each charge state in a given PL spectrum (c_0, c_-) are determined by our fitting the acquired spectrum $I(\lambda)$ to a linear combination of N-V^- and N-V^0 emission:

$$I(\lambda) = M\Big[c_-\hat{I}_-(\lambda) + c_0\hat{I}_0(\lambda)\Big]. \tag{2}$$

Here M is a proportionality constant, and $\hat{I}_-(\lambda)$ and $\hat{I}_0(\lambda)$ denote area-normalized PL spectra for N-V^- and N-V^0, respectively; the normalization satisfies $\int_\lambda \hat{I}_-(\lambda)d\lambda = 1$ and $\int_\lambda \hat{I}_0(\lambda)d\lambda = 1$, where the integral is taken over the wavelengths measured by the spectrometer. Throughout this paper, the hat denotes dimensionless spectra that are normalized to unity area.

We now describe the process used to determine $\hat{I}_0(\lambda)$ and $\hat{I}_-(\lambda)$, the accuracies of which are critical for the decomposition denoted in Eq. (2) to be effective. PL spectra are recorded for all 28 diamonds using 18 different 532-nm-optical-excitation intensities between 1 kW/cm^2 and 4 MW/cm^2 (see Appendix B 2 for intensity calculations). The PL spectra are area-normalized and sorted by the fractional PL contribution in the 560–600-nm band, which includes the N-V^0 zero-phonon line (ZPL) at 575 nm. The area-normalized PL spectrum with the greatest 560–600-nm content is denoted $\hat{I}_0^{\text{pre}}(\lambda)$ and the area-normalized PL spectrum with the least 560–600-nm content is denoted $\hat{I}_-^{\text{pre}}(\lambda)$. The superscript "pre" denotes the spectra are preliminary and require additional processing, as now described. The spectra $\hat{I}_0^{\text{pre}}(\lambda)$ and $\hat{I}_-^{\text{pre}}(\lambda)$ are nominally dominated by PL from N-V^0 and N-V^-, respectively. Postanalysis investigation shows $\hat{I}_0^{\text{pre}}(\lambda)$ contains approximately 94% N-V^0 emission and approximately 6% N-V^- emission, while $\hat{I}_-^{\text{pre}}(\lambda)$ contains approximately 84% N-V^- emission and approximately 16% N-V^0 emission. We assume that PL from other defects (Si-V, V^0, etc.) can be ignored; no ZPLs from such defects are observed for irradiation doses of approximately 10^{19} e^-/cm^2 or less.

The un-normalized N-V^- $I_-(\lambda)$ function is constructed with

$$I_-(\lambda) = \hat{I}_-^{\text{pre}}(\lambda) - \delta_0\hat{I}_0^{\text{pre}}(\lambda), \tag{3}$$

where the value of δ_0 is adjusted so that $I_-(\lambda)$ exhibits no evidence of the N-V^0 ZPL feature at 575 nm. The $I_-(\lambda)$ function is then area-normalized to yield $\hat{I}_-(\lambda)$. The $\hat{I}_-(\lambda)$ function is determined to be free of any N-V^0 contribution to the 1% level or below (see Appendix C 3). The un-normalized N-V^0 $\hat{I}_0(\lambda)$ function is then similarly constructed with

$$I_0(\lambda) = \hat{I}_0^{\text{pre}}(\lambda) - \delta_-\hat{I}_-(\lambda), \tag{4}$$

where the value of δ_- is adjusted so the resulting $I_0(\lambda)$ exhibits no evidence of the N-V^- ZPL feature at 637 nm. This $I_0(\lambda)$ function is then area-normalized to yield $\hat{I}_0(\lambda)$. Ensuring the $\hat{I}_0(\lambda)$ function is free of any N-V^- contribution is nontrivial; the N-V^- ZPL coincides with near-peak N-V^0 vibronic sideband emission and is thus difficult to isolate and remove. Nevertheless, δ_- is determined to be $(6.4 \pm 3.3)\%$, suggesting the resultant $\hat{I}_0(\lambda)$ function should exhibit at most a small contribution on the order of a few percent from N-V^-. The extracted $\hat{I}_-(\lambda)$ and $\hat{I}_0(\lambda)$ functions for bulk N-V diamond [34] are shown in Figs. 1 and 2, respectively.

As an independent check of the extracted $\hat{I}_-(\lambda)$ basis function, we adjust the low-temperature, one-phonon emission spectrum of the $^3A_2 \leftarrow {}^3E$ transition [28] for higher temperatures and multiphonon transitions, as outlined in Ref. [35]. Specifically, the 300-K trace in Fig. 8 in Ref. [35] is digitized [36] and adjusted by the necessary ω^3 weighting [32] to yield an expected room-temperature PL spectrum (less any ZPL contribution). The results are shown in Fig. 1, and are in good agreement with our experimental determination of $\hat{I}_-(\lambda)$. As the spectrum derived from Ref. [35] excludes the ZPL contribution, a comparison of the expected and measured data yields residuals whose main feature is the N-V^- ZPL; these residual data are well fit by a Lorentzian with a Debye-Waller factor of 4.3 and a full-width-at-half-maximum linewidth of 2.6 nm.

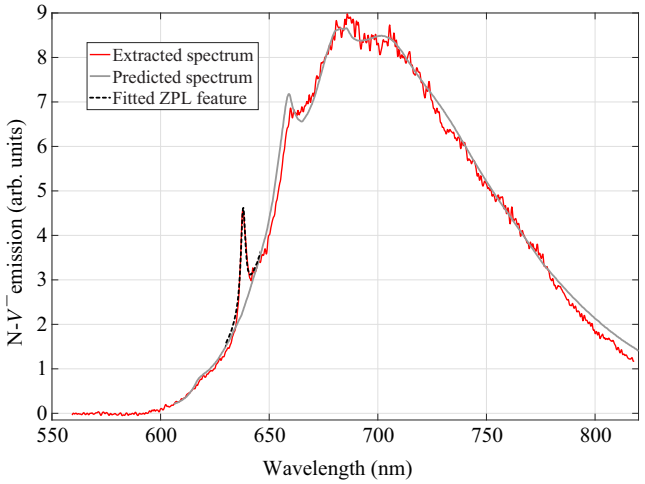

FIG. 1. N-V^- photoluminescence. Extracted and predicted N-V^- photoluminenscence spectra at room temperature as described in the main text. The extracted and predicted curves are in good agreement. The ZPL feature itself included here is not predicted *a priori* but is consistent with the range of ZPL parameters found in the literature.

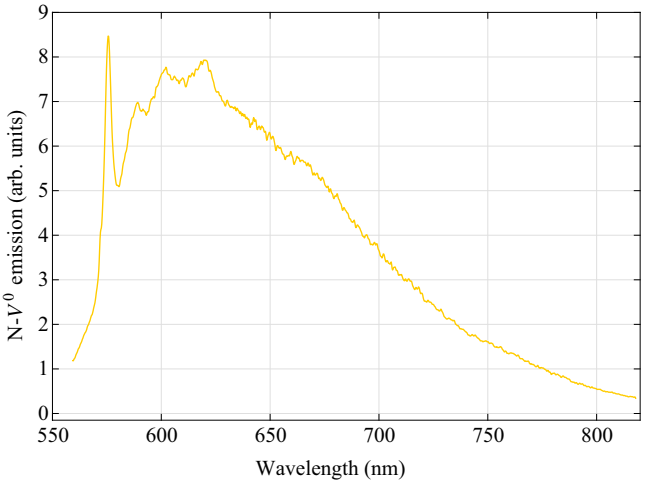

FIG. 2. N-V^0 photoluminescence. Extracted N-V^0 photoluminescence spectrum at room temperature as described in the main text.

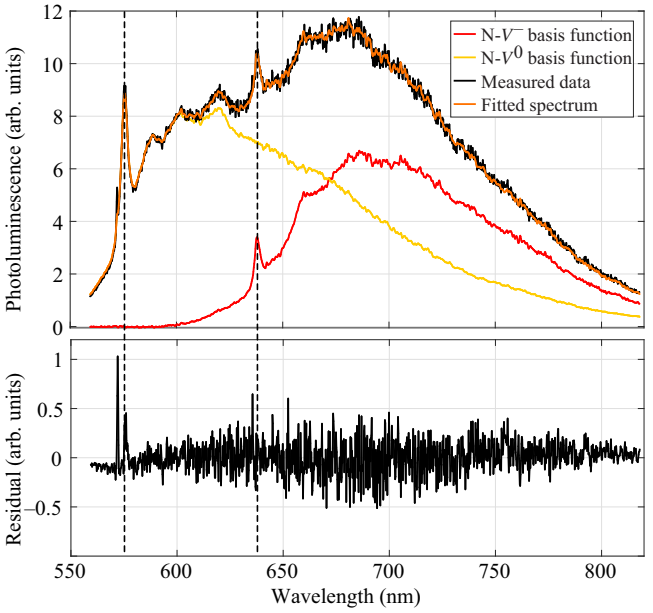

FIG. 3. Example decomposition of diamond photoluminescence spectra. The top panel shows PL spectra for sample F, decomposed as a linear combination of the N-V^0 and N-V^- PL spectra. The fit to the total PL is also shown. Residuals between the measured and fit data in the top panel are shown in the bottom panel. In both panels, the dashed black vertical lines indicate the position of the N-V^0 and N-V^- ZPLs at 575 and 637 nm, respectively.

These values are well within the range of values reported in the literature [1] (see Table II).

Using the determined $\hat{I}_-(\lambda)$ and $\hat{I}_0(\lambda)$ basis functions, we decompose the PL spectra for all 28 diamonds at the 18 optical excitation intensities investigated via Eq. (2). An example decomposition is shown in Fig. 3. To verify our approach, we compare the photoluminescence-decomposition-analysis (PDA) method presented here with the Debye-Waller decomposition and observe that the PDA method is more robust to noise and produces more-consistent results (Fig. 4). This improvement is likely due to the PDA method harnessing the entire approximately-200-nm PL spectrum, compared with the Debye-Waller decomposition, which uses data only in the ZPL vicinity (a few nanometers). Further information on the Debye-Waller decomposition is provided in Appendix C 2. As an additional benefit, the PDA method does not require *a priori* knowledge of the Debye-Waller factors, which are observed to differ in the literature (see Table II).

B. Charge-state photoluminescence ratio

Accurate determination of the charge-state efficiency ζ using Eq. (1) requires first determining κ_{532}, the relative PL rate of N-V^- to N-V^0 under low-intensity (i.e., well below saturation for either species) 532-nm optical excitation. Equivalently, κ_λ can be formally defined as

$$\kappa_\lambda = \left[\frac{\int_{\lambda'} I_-(\lambda')d\lambda'}{\int_{\lambda'} I_0(\lambda')d\lambda'}\right]_{[\text{N-}V^0]=[\text{N-}V^-]}, \tag{5}$$

where κ_λ is evaluated in the low-optical-excitation-intensity limit.

We estimate the value of κ_{532} using three independent methods. First, the total integrated PL is given by the following proportionality:

$$\int_\lambda I(\lambda)\, d\lambda \;\propto\; \left([\text{N-}V^0] + [\text{N-}V^-]\kappa_{532}\right)\frac{2P}{\pi w_0^2}, \tag{6}$$

where P and w_0 are the optical excitation power at the confocal volume and the $1/e^2$ intensity radius at the origin, respectively. The factor $2P/\pi w_0^2$ corresponds to the peak intensity of the exciting laser beam (see Appendix B 2). The N-V^0 and N-V^- concentrations are constrained at any given time to satisfy

$$[\text{N-}V^0] + [\text{N-}V^-] = \text{constant} \tag{7}$$

for a given sample. Equation (7) implicitly assumes the concentration of positively charged N-V centers can be ignored. Even well below saturation intensity, the concentration ratio of N-V^- to N-V^0 varies as a function of the applied 532-nm optical excitation intensity, as shown in Fig. 4. Therefore, by varying the 532-nm optical excitation intensity to vary the concentration ratio of N-V^- to N-V^0, we can determine the value of κ_{532}. This method is used for seven diamonds where $c_0 \approx c_-$ for 532-nm laser intensities below 20 kW/cm^2 (i.e., well below saturation). Analyzing the combined data, we extract the relative PL rate of N-V^- to N-V^0 to be $\kappa_{532} = 2.5 \pm 0.5$.

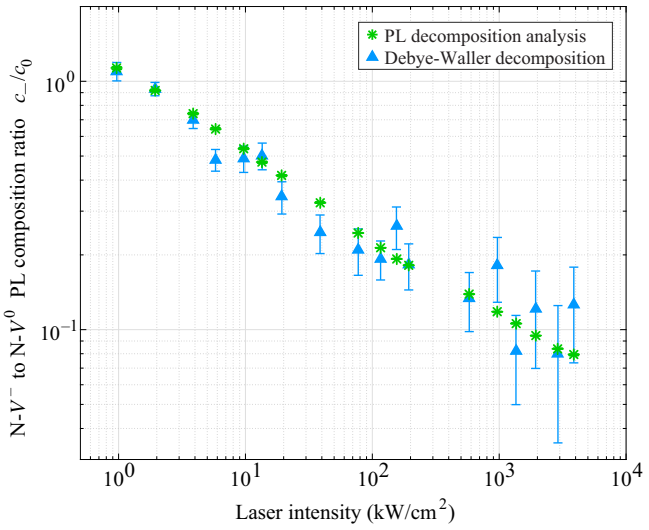

FIG. 4. Comparison of methods determining the PL composition ratio c_-/c_0 for sample S. The PL composition ratio c_-/c_0 is determined by both photoluminescence decomposition analysis and Debye-Waller decomposition for various laser intensities. Both methods analyze the same data. The photoluminescence decomposition analysis produces c_-/c_0 ratios that are more consistent across laser intensities and have smaller error bars.

Second, the value of κ_{532} derived as described above is checked with third-party data, where the concentration ratio of N-V^- to N-V^0 is varied by electrical control. Kato *et al.* [23] fabricated N-V centers inside the insulating layer of a diamond-based p-i-n-junction diode. By adjusting the bias voltage applied across the device, they directly controlled the concentration ratio of N-V^- to N-V^0 (see Ref. [23], Fig. 4). Using PL spectra taken for a variety of bias voltages (obtained directly from the authors of Ref. [23]), we estimate the charge-state PL ratio κ_{532} (see Appendix C 4). This secondary method finds $\kappa_{532} = 2.17$. We note that this method implicitly assumes that the electric field used to vary the concentration ratio of N-V^- to N-V^0 does not affect the dynamics of N-V^- or N-V^0 beyond their charge-state ratio. Both methods implicitly assume that the sum of the concentrations of N-V^0 and N-V^- is conserved.

Third, as a final check on the value of κ_{532} determined, we evaluate the concentration ratio of N-V^- to N-V^0 for a test diamond not part of the rest of this study. UV-vis measurements on this diamond suggest a concentration ratio of N-V^- to N-V^0 of 1.33 ± 0.2. PL measurements at intensities of 1 and 2 kW/cm^2 find the c_-/c_0 ratio to be 2.6 and 2.1 respectively; a linear extrapolation (which we note is likely to underestimate c_-/c_0) to zero illumination suggests $c_-/c_0 = 3.1$ in the dark. This analysis yields an estimate of $\kappa_{532} = 2.3 \pm 0.2$, although we note this linear extrapolation is likely to underestimate the actual value of κ_{532}. As all three methods are in good agreement, we estimate $\kappa_{532} = 2.5 \pm 0.5$.

The determination of the relative florescence ratios of N-V^- to N-V^0 is expected to aid in uncovering presently unknown dynamics of the N-V^0 center, which is less well studied than the N-V^- center. For example, this ratio may help determine the stimulated-emission cross section or the radiative quantum efficiency of the N-V^0 $^2A_2$ state.

V. ANNEALING AND NITROGEN-CONVERSION STUDY

For CVD-grown diamonds, the fraction of total nitrogen incorporated as N-V centers during growth is typically quite low, with reported values ranging roughly from 0.0007 to 0.03 [7,37]. As discussed previously, this low as-grown N-V conversion efficiency χ can be increased through electron irradiation and subsequent annealing. At the MeV-level energies typically used in electron irradiation, N-V creation via this mechanism depends significantly on the irradiation dose, with behavior that can be simply described in the following three regimes:

(a) For irradiation doses that introduce substantially fewer vacancies than the grown-in native N-V population, the observed quantity [N-V^T] is predominantly independent of the electron irradiation dose D_e.

(b) At very high irradiation doses, the quantity [N-V^T] saturates as every nitrogen is paired with a vacancy (to an order-unity correction factor [7]).

(c) At certain intermediate irradiation doses, the value of [N-V^T] is expected to vary linearly with the electron irradiation dose D_e [7]. In this regime, N-V centers created by irradiation and annealing outnumber the native N-V centers, yet $[V] \ll [\mathrm{N}^T]$, so a given additional vacancy is expected to create an additional N-V center.

We propose a simple phenomenological model to approximate N-V annealing dynamics consistent with the above three limiting cases:

$$[\text{N-}V^T] = [\text{N-}V^T]_{\text{gro}} + \left(F_c[\mathrm{N}^T] - [\text{N-}V^T]_{\text{gro}}\right)\left(1 - e^{-\frac{BD_e}{F_c[\mathrm{N}^T]-[\text{N-}V^T]_{\text{gro}}}}\right), \tag{8}$$

where $[\text{N-}V^T]_{\text{gro}}$ is the total native N-V concentration immediately following growth (i.e., before irradiation and annealing), B is the vacancy creation rate per unit length, and the constant F_c accounts for the empirical observation that $[\text{N-}V^T]/[\mathrm{N}^T]$ saturates at 0.6 ± 0.07 [7] in the limit of high irradiation dose. The following analysis therefore uses the estimate $F_c = 0.6$ with the caveat that the true value of F_c likely depends on the underlying diamond material and annealing conditions. For the diamonds in this study, $[\mathrm{N}^T] \gtrsim 100 \times [\text{N-}V^T]_{\text{gro}}$; as a result, Eq. (8) may be

simplified to [37]

$$[\text{N-}V^T] \approx [\text{N-}V^T]_{\text{gro}} + F_c[\text{N}^T]\left(1 - e^{-BD_e/F_c[\text{N}^T]}\right). \quad (9)$$

To test the validity of Eq. (9), a correlate of the quantity $[\text{N-}V^T]$ is determined for each diamond as described herein. For each diamond, the PL spectrum is recorded under nonsaturating 532-nm illumination (20 kW/cm^2 or less) and is decomposed into the N-V^- and N-V^0 components (see Sec. IV A). Using the relative charge-state PL ratio κ_{532} at low excitation intensity and the fractional distribution between N-V^- and N-V^0 in the PL (c_0, c_-), we adjust the PL contributions into a correlate of $[\text{N-}V^T]$. That is, we set $[\text{N-}V^T] = A(c_- + \kappa_{532}c_0)$, where A is proportional to the total PL. Such treatment is expected to be justified in the low-intensity limit where the PL of N-V^- and the PL of N-V^0 are both proportional to the optical excitation intensity (see Appendix B 2). An example plot depicting the total N-V concentration for all 28 diamonds is shown in Fig. 5 for a 532-nm intensity of 6 kW/cm^2.

The annealing data shown in Fig. 5 illustrate that for intermediate irradiation doses of approximately 10^{17} e^-/cm^2, the 1250 °C 1-h anneal was more effective in creating N-V centers than the 850 °C 1-h anneal. The results suggest that 850 °C 1 h anneal was insufficient for most vacancies to diffuse to a substitutional nitrogen. In a simple model where non-nitrogen-vacancy traps are ignored, we measure an approximate diffusion coefficient D of 1.8 nm^2/s (see Appendix D 2 for additional details).

Examination of the fit parameters in the phenomenological model given by Eq. (9) can give further information about the annealing and irradiation process. In particular,

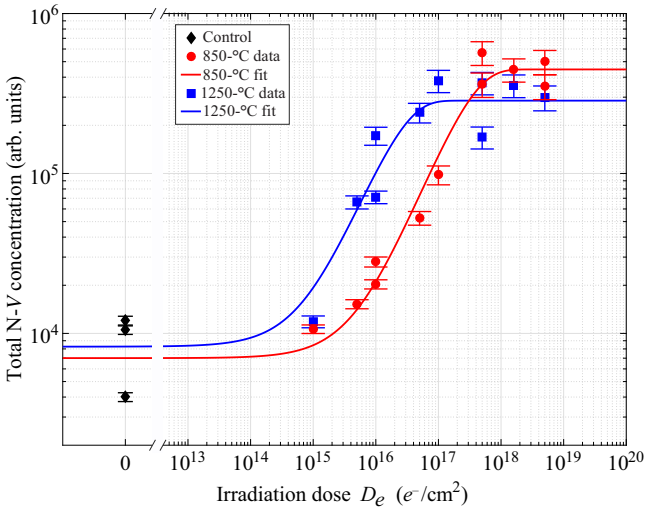

FIG. 5. Total N-V concentration versus irradiation dose D_e. Data are shown for unirradiated control diamonds (♦), diamonds annealed at 850 °C (●), and diamonds annealed at 1250 °C (■). Error bars denote the standard deviation of multiple measurements on the same sample.

the data for samples annealed at 1250 °C corresponds to a fitting parameter of $B = 0.52 \pm 0.26$ cm^{-1} for $[\text{N}^T] = 118$ ppb. This value of B represents the vacancy creation rate for electron irradiation at 1 MeV when all recombination, including that occurring during subsequent annealing, is accounted for. The value of B determined here is approximate; if there are substantial vacancy sinks, the value of B obtained will underestimate the true vacancy creation rate. However, conversely, the value of B can then be used as a probe of the prevalence of vacancy sinks in diamond material of interest. Finally, we note that the value of B obtained here falls within the range of values reported in the literature, 0.2 to 1.5 cm^{-1} for electron energies between 1 and 5 MeV. Independent measurements by UV-vis spectroscopy suggest a vacancy creation rate of 0.30 ± 0.05 cm^{-1}, consistent with the measured value of B. See Appendix D 1 for further discussion.

Additionally, Fig. 5 shows that the fits for the 850- and 1250 °C anneals asymptote to different values of $[\text{N-}V^T]$, with the former resulting in a value approximately 50% higher than the latter. A comparison-of-means test yields a p value of 0.05. Statistical significance aside, one plausible interpretation is that the increased mobility of one or more species at 1250 °C is detrimental to the formation (or preservation) of N-V centers. Another plausible hypothesis is that N-V formation is less favorable at higher temperatures due to thermochromic charge-transfer effects [7].

VI. T_1 AND T_2 RELAXATION STUDY

Following initialization into a given spin state, N-V spins relax into the thermally mixed state from spin-lattice-induced interactions or other mechanisms [14]. The characteristic T_1 longitudinal relaxation time is particularly relevant for T_1 relaxometry measurements [38–40]. The value of T_1 is evaluated for a randomly selected diamond subset (14 of the 28 samples) after irradiation and annealing. All 14 diamond samples exhibit values of T_1 between 4.8 and 6.5 ms. For doses of 5×10^{18} e^-/cm^2 or less, the data suggest T_1 exhibits little if any dependence on irradiation dose, as shown in Fig. 6.

The T_2 coherence time is an important parameter for ac magnetometry [41,42], quantum information [43,44], nanoscale NMR [45–52], single-protein sensing [53], and other applications involving N-V-diamond quantum sensors. T_2 of a given species is determined in part by the surrounding paramagnetic spin bath [54–57], and can be approximated as

$$\frac{1}{T_2} \simeq \sum_X \frac{1}{T_{2,\text{N-}V^-/X}} + \frac{1}{2T_1}, \quad (10)$$

where $T_{2,\text{N-}V^-/X}$ corresponds to the T_2 coherence time limited by N-V^- dipolar interactions with species X, T_1

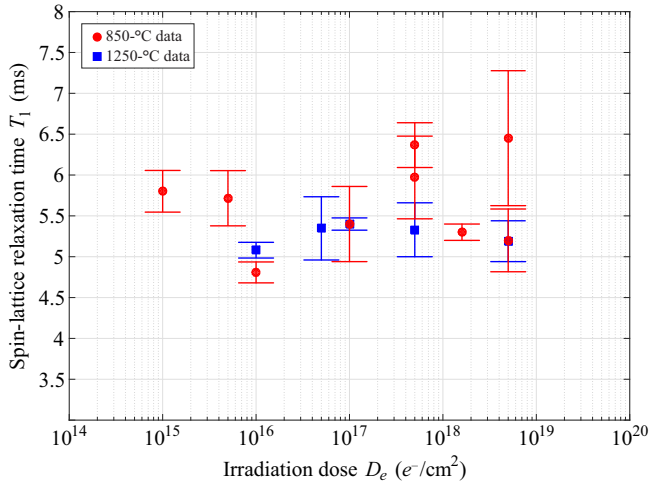

FIG. 6. T_1 versus irradiation dose D_e. Data are shown for diamonds annealed at 850 °C (●) and diamonds annealed at 1250 °C (■). The measured value of T_1 displays little if any dependence on either irradiation dose or annealing temperature for irradiation doses $D_e \leq 5 \times 10^{18}$ e/cm^2. Error bars denote the standard deviation of multiple meausurements on the same sample.

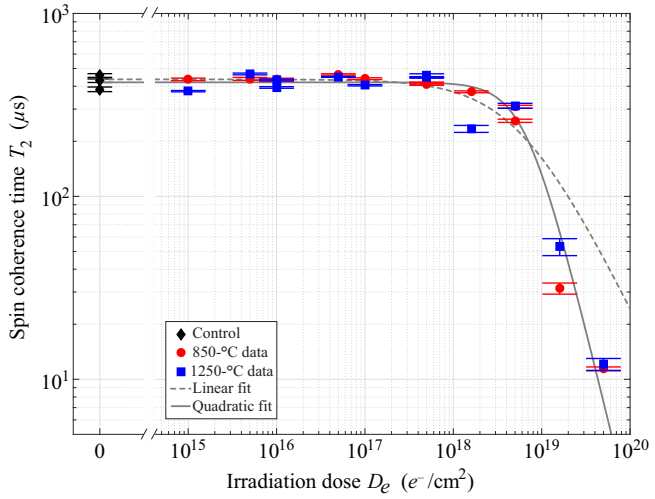

FIG. 7. T_2 versus irradiation dose D_e. Data are shown for unirradiated control diamonds (♦), diamonds annealed at 850 °C (●), and diamonds annnealed at 1250 °C (■). Little if any decrease in T_2 is observed for irradiation doses D_e approximately less than 10^{18} e/cm^2. The data are fit to two models, one where T_2 decoherence is linearly proportional to the dose (---) and another where T_2 decoherence is quadratic with the dose (—) as described in the main text. Error bars denote the standard deviation of multiple measurements on the same sample.

is the longitudinal relaxation time [58], and the summation is evaluated over all paramagnetic species X in the diamond. Similarly to ion implantation [59–62], the electron-irradiation process can introduce paramagnetic impurities into the diamond lattice [63], which degrade the T_2 coherence time. While annealing can partially mitigate this damage, empirical observations suggest some lattice damage will always remain [60,64–67]. Therefore, the irradiation doses at which T_2 and T_1 are compromised are quantities of interest for many applications using N-V ensembles.

T_2 is measured for all 28 diamonds using a Hahn-echo sequence (see Appendix E) and is plotted versus irradiation dose in Fig. 7. To characterize the effects of the irradiation dose D_e and annealing on T_2, the data are first fit to a linear model of the form $1/T_2 = (1/W_1)(1 + D_e/W_2)$. We determine $W_1 = 436 \pm 11$ μs, which can be interpreted as the T_2 value in the absence of irradiation. However the poor fit of this *linear model* at higher irradiation doses suggests the model does not capture the relevant dynamics. Instead, fitting the data to the *quadratic model* $1/T_2 = (1/W_1)(1 + D_e^2/W_3^2)$ produces a better fit. This fit does not improve with addition of a term linear in D_e. The best-fit parameters for this quadratic model are $W_1 = 420 \pm 10$ μs and $W_3 = 6.8 \pm 0.8 \times 10^{18}$ cm^{-2}. The value of W_3 may be interpreted as the irradiation dose that decreases T_2 by 2 times relative to the unirradiated value $T_2 = W_1$.

Given that $W_3 \sim 400 \times \langle D_e^{3\,\mathrm{dB}} \rangle$, where $\langle D_e^{3\,\mathrm{dB}} \rangle = 1.6 \pm 0.8 \times 10^{16}$ cm^{-2} is the dose that converts half the initial nitrogen concentration to N-V centers as determined from the phenomenological model, the data suggest any desired N-V conversion (i.e., [N-V]/[N^T]) can be obtained with negligible decrease in T_2 from irradiation-induced defects. The failure of the linear model at the highest doses suggests the dominant source of decoherence observed at high doses is not the negatively charged vacancy (at least under the simplifying assumption that a given vacancy's charge state is independent of dose). Further study is required to isolate the decoherence mechanism responsible.

VII. SUMMARY AND OUTLOOK

In this work, we present a room-temperature, all-optical technique for rapidly and quantitatively characterizing the N-V^--to-N-V^0 charge-state ratio. In particular, we isolate the emission spectra of N-V^- and N-V^0, allowing arbitrary diamond spectra to be decomposed into a linear combination of the N-V^- and N-V^0 spectral contributions. This photoluminescence decomposition analysis exhibits better reproducibility and lower noise than the Debye-Waller-factor approach and does not require multiple excitation wavelengths [26]. Furthermore, to enable the *quantitative* extraction of the N-V^--to-N-V^0 charge-state ratio from these PL measurements, we also empirically determine the relative PL rate of N-V^- compared with that of N-V^0, finding $\kappa_{532} = 2.5 \pm 0.5$ under low-intensity 532-nm excitation.

In addition to providing an expedient method to optimize irradiation and annealing of N-V-diamond material targeting high-performance quantum-sensing applications,

the PDA technique and analyses presented are expected to help uncover unknown or poorly understood N-V-diamond behavior. For example, κ_λ can likely be used to place bounds on the branching ratios and quantum efficiency of the N-V^0 $^2E \leftrightarrow {}^2A_2$ transition. Further, extensions of the PDA technique may be used to measure N-V^- and N-V^0 saturation intensities, which are not precisely known and may vary for N-V ensembles in different strain or charge environments, where reported branching ratios differ [68–70]. Finally, extending the findings of this work—through additional study of vacancy creation, diffusion, and annealing, as well as through further investigation of the mechanism for the N-V^- T_2 spin-coherence time's quadratic dependence on the irradiation dose—is expected to provide useful insight into the defect content of different diamond materials. Using these techniques and analyses to develop a more-comprehensive understanding of diamond-material composition and the effects of processing thereon is critical for advancing quantum sensing based on ensembles of N-V centers in diamond.

ACKNOWLEDGMENTS

We gratefully acknowledge the authors of Ref. [23], Hiromitsu Kato, Marco Wolfer, Christoph Schreyvogel, Michael Kunzer, Wolfgang Müller-Sebert, Harald Obloh, Satoshi Yamasaki, and and Christoph Nebel, for providing raw data allowing us to confirm the measured value of κ_{532}. We thank Daniel Twitchen for insights into literature variation in irradiation outcomes. The Lincoln Laboratory portion of this work is supported by the Under Secretary of Defense for Research and Engineering under Air Force Contract No. FA8702-15-D-0001. S.A. was supported by the National Science Foundation (NSF) through the NSF Graduate Research Fellowships Program. P.C. acknowledges support from the ARO MURI on Qubit Enabled Imaging, Sensing & Metrology (W911NF-11-1-0400).

Any opinions, findings, conclusions or recommendations expressed in this material are those of the author(s) and do not necessarily reflect the views of the Under Secretary of Defense for Research and Engineering.

APPENDIX A: DIAMOND CHARACTERISTICS

1. Diamond nitrogen-concentration estimation

The primary contributors to N-V^- T_2 coherence times are ^{13}C, residual neutral nitrogen, and spin-lattice interactions (i.e., T_1-related processes). Consequently, Eq. (10) can be used to estimate the value of $[N^T]$. The data in Fig. 7 suggest $T_2 = 420 \pm 10$ μs for unirradiated diamonds in our study. From Ref. [55] we expect $T_{2,\text{N-}V^-/\text{N}} = 165 \pm 15\,\text{ppm} \times \mu\text{s}$, where $[N^T]$ is evaluated in parts per million (i.e., a diamond with $[N^T]$ = 1 ppm will have $T_{2,\text{N-}V^-/\text{N}} = 165$ μs, while a diamond with $[N^T]$ = 2 ppm will have $T_{2,\text{N-}V^-/\text{N}} = 165/2$ μs ≈ 83 μs). For the ^{13}C decoherence contribution, we use values reported in the literature for samples exhibiting natural isotopic abundance: Hall *et al.* [71] theoretically predicted 780 μs; Mizuochi *et al.* [72] measured 650 μs for a single N-V; Balasubramanian *et al.* [73] measured 1.8 ms for an N-V in 0.3% ^{13}C diamond, which corresponds to T_2 of 504 μs for natural-abundance ^{13}C; and Stanwix *et al.* [74] reported 600 μs for N-V ensembles in high-purity diamonds with a natural abundance of ^{13}C. Taking the average of these four values yields $T_{2,\text{N-}V^-/^{13}\text{C}} = 634 \pm 114$ μs for diamonds with natural-abundance ^{13}C. We evaluate T_1 from Fig. 6, which yields $T_1 = 5.5 \pm 0.5$ ms, and this is in good agreement with data presented in Ref. [58]. Use of Eq. (10) with the above estimates suggests a mean total nitrogen concentration of approximately 118 ± 48 ppb for the diamonds studied here.

This estimate is consistent with measurements reported in Ref. [75] for standard-grade diamonds from Element Six. Test results for 20 diamonds of the same part number exhibited a mean nitrogen concentration of 120 ppb with a standard deviation of 16 ppb and minimum and maximum concentrations of 95 and 162 ppb, respectively [75]. Since the nitrogen concentration strongly affects the CVD-diamond growth rate, optical absorption, and other diamond properties, this parameter is carefully controlled during diamond growth, and it is perhaps unsurprising that the diamond samples used in this work exhibit similar nitrogen concentrations.

2. Irradiation parameters

Diamonds were electron-irradiated by a commercial supplier (Prism Gem LLC). The electron energy of the Van de Graaff accelerator was fixed at 1 MeV. For a dose of 1×10^{15} e^-/cm^2, a beam current of 2.5 mA is used for 36 s, for doses of 1×10^{16} and 1×10^{17} e^-/cm^2, a beam current of 2.5-mA is used for 6 min and 1 h, respectively, and for doses of 1×10^{18} and 1×10^{19} e^-/cm^2, a beam current of 25 mA is used for 1 and 10 h, respectively. Irradiation doses are calculated by the formula $D_e = It/Aq_e$, where I is the beam current, A is the scan area over which the electron beam is rastered, q_e is the electron charge, and t is the irradiation time. Table I details the irradiation doses for the 28 diamonds used in this study.

APPENDIX B: EXPERIMENTAL DETAILS

1. Confocal microscope

A homebuilt confocal microscope, shown diagrammatically in Fig. 8, allows PL spectroscopy and coherence measurements of the diamond samples. Green 532-nm laser light (Coherent Verdi G5) is sent through an acousto-optic modulator (Crystal Technology/Gooch & Housego 3200-147). The zeroth-order beam is discarded, while the first-order beam passes through a half-wave plate, reflects

TABLE I. Electron-irradiation and annealing parameters for diamonds used in this study. Variables include an optional 850 °C 1-h anneal before irradiation, a 1-MeV electron-irradiation dose D_e, a postirradiation 850 ° C anneal for 1 h, and an optional second anneal at 1250 °C for 1 h.

Sample	Preanneal, 1 h (°C)	Irradiation dose at 1 MeV (e^-/cm^2)	First anneal, 1 h (°C)	Second anneal, 1 h (°C)
C1	None	None	None	None
C2	None	None	None	None
C3	850	None	850	None
A	850	1.0×10^{15}	850	None
B	850	5.0×10^{15}	850	None
C	850	1.0×10^{16}	850	None
D	850	1.0×10^{16}	850	None
E	850	5.0×10^{16}	850	None
F	850	1.0×10^{17}	850	None
G	850	5.0×10^{17}	850	None
H	850	5.0×10^{17}	850	None
I	850	1.6×10^{18}	850	None
J	850	5.0×10^{18}	850	None
K	None	5.0×10^{18}	850	None
L	850	1.6×10^{19}	850	None
M	850	5.0×10^{19}	850	None
N	850	1.0×10^{15}	850	1250
O	850	5.0×10^{15}	850	1250
P	850	1.0×10^{16}	850	1250
Q	850	1.0×10^{16}	None	1250
R	850	5.0×10^{16}	None	1250
S	850	1.0×10^{17}	None	1250
T	850	5.0×10^{17}	None	1250
U	850	5.0×10^{17}	None	1250
V	850	1.6×10^{18}	850	1250
W	850	5.0×10^{18}	None	1250
X	850	1.6×10^{19}	850	1250
Y	850	5.0×10^{19}	850	1250

off a dichroic mirror, and is focused onto the diamond with a commercial microscope objective (Mitutoyo M Plan Apo 20× 378-804-3) with 0.42 NA, focal length $f_{\mathrm{obj}} = 10$ mm, and back aperture $D_{\mathrm{BA}} = 8.4$ mm. A permanent magnet mounted on a translation stage creates a static bias magnetic field of moderate strength (40–60 G) aligned along one of the four diamond crystallographic directions, allowing individual addressing of the magnetic resonances associated with the N-V subensemble oriented along the bias field. This bias-field alignment prevents T_2 measurements from being skewed by the effects of ^{13}C.

The diamond is mounted over a hole in a 170-μm-thick glass coverslip attached to a stainless-steel ring (Thorlabs RS1M). Microwaves are applied to the diamond from above using a loop antenna. For T_2 and T_1 measurements, the interrogation volume is located at the top of the diamond, closest to the microwave loop, to achieve maximum microwave drive strength. For PL measurements, the interrogation volume is located near the bottom diamond surface to minimize spherical aberration effects from the diamond's refractive index $n_d \approx 2.41$.

Light emitted from the N-V ensemble is collected by the 20× objective and subsequently coupled with use of a 200-mm-focal-length lens into 10-μm-core multimode fiber (Thorlabs M64L02) that serves as a pinhole. This fiber is connected to either a spectrometer (Princeton Instruments IsoPlane SCT 320) for photoluminescence measurements or a fiber connected to an avalanche-photodiode single-photon counter (Excelitas SPCM-AQRH-FC). The spectrometer is both wavelength and intensity calibrated (Princeton Instruments Intelical). The intensity calibration removes instrumental artifacts in the PL spectra that arise from the differing spectral responses from various optical elements in the spectrometer (mirrors, diffraction grating, CCD camera, etc.). Counts registered by the single-photon counter are recorded by a data-acquisitions card (National Instruments PCIe-6251), which is in turn gated by a pulse generator (SpinCore PulseBlasterESR-PRO). The pulse generator is used to gate the optical excitation, microwave radiation, and single-photon-counter measurement.

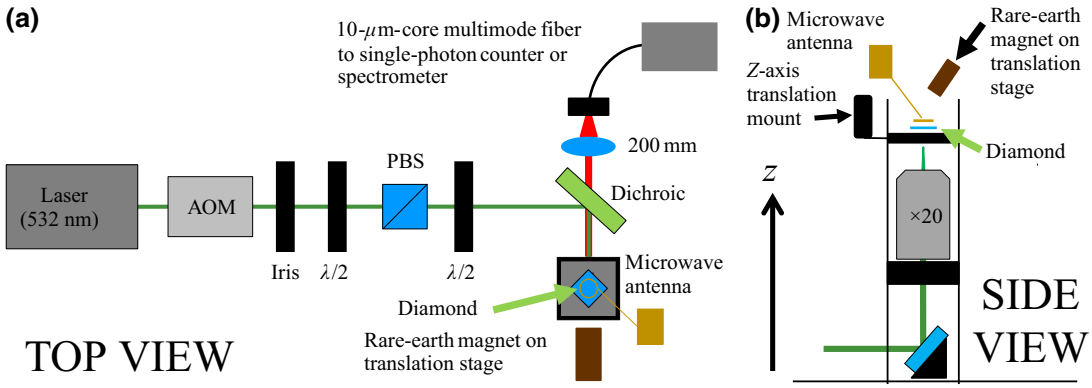

FIG. 8. Overview of the experimental setup. (a) Top-down schematic of the confocal microscope detailing the excitation and collection optics. The optical system is designed so that the numerical aperture of the collection (red) is greater than the numerical aperture of the excitation (green), allowing PL collection from only the center of the excitation volume. (b) Vertical view of the confocal microscope close to the diamond.

2. Intensity calculations and saturation

To calculate the intensity associated with a given excitation laser power, we model the intensity of the green laser beam focused by the objective as a Gaussian profile:

$$I(r,z) = \frac{2P}{\pi w(z)^2} \exp\left(-\frac{2r^2}{w(z)^2}\right), \tag{B1}$$

where P is the incident 532-nm power corrected for any transmission losses, $w(z) = w_0\sqrt{1+(z/z_R)^2}$ is the $1/e^2$-intensity radius, $z_R = \pi n_d w_0^2/\lambda$ is the Rayleigh range (adjusted for the diamond index of refraction n_d), r is the radial distance in the plane transverse to the beam, λ is the wavelength in free space, and z is the axial distance from the origin, defined as the center of the collection volume [76]. The $1/e^2$-intensity diameter at the origin is $2w_0$. The peak intensity I_0 is given by

$$I_0 = \frac{2P}{\pi w_0^2}. \tag{B2}$$

A beam profiler (Newport LBP2-HR-VIS) measures the spot size of the Gaussian laser beam immediately before the objective to be about 2.25 mm in diameter ($1/e^2$). For an input diameter $D_{\text{in}} = 2.25$ mm, laser wavelength $\lambda = 532$ nm, and objective focal length $f_{\text{obj}} = 10$ mm, the focused-excitation-beam waist is $w_0^{\text{ex}} = 2\lambda f_{\text{obj}}/\pi D_{\text{in}} = 1.5\ \mu$m [76]. This yields a Rayleigh range $z_R = 32\ \mu$m for the excitation beam.

The saturation intensity of the N-V^- center is on the order of 100 kW/cm^2 [2], with the saturation intensity of the N-V^0 center likely to be higher. For measurements relating collected PL to total N-V concentration, excitation intensities of 3.3 kW/cm^2 or less were used.

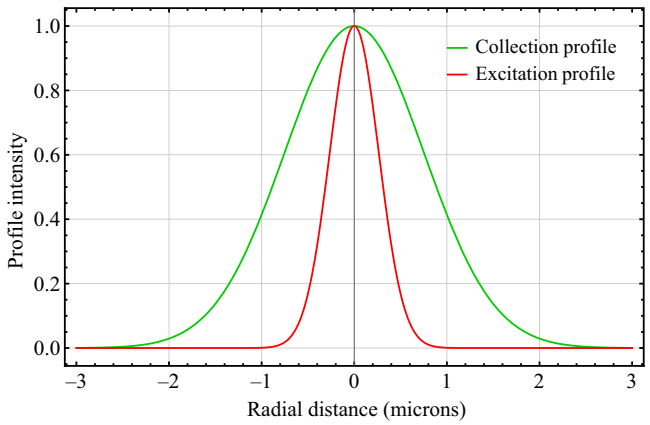

FIG. 9. Radial excitation and collection profiles at the center of the confocal volume. The collection profile for 700-nm light is made smaller than the 532-nm excitation profile to allow PL collection only from N-V centers with near-uniform optical illumination intensity.

3. Excitation and collection volume

Interpretation of photoluminescence and related derived data is most straightforward if the interrogated N-V centers receive near-uniform optical excitation intensity. To ensure that the N-V centers in the collection volume are near-uniformly illuminated with 532-nm light, the collection volume is restricted to the central region of the excitation volume. In contrast to the 532-nm excitation, the collection of fluorescence makes full use of the objective 0.42 numerical aperture. As the objective back aperture D_{BA} is 8.4 mm, the collection beam waist is $w_0^{\text{col}} = \frac{2\lambda f_{\text{obj}}}{\pi D_{\text{BA}}}$, which is 0.53 μm for 700-nm light. A radial slice of the excitation and collection profiles is shown in Fig. 9.

TABLE II. Debye-Waller factors for N-V^- as reported in the literature.

N-V^- Debye-Waller factor $\tilde{S}$	Temperature (K)	Diamond type	Reference
2.65	~ 4	Ensemble, Ib	[33]
4.7	300	Ensemble, Ib	[33]
4.79, 4.25, 2.79	Room temperature	Single N-V centers	[79]
3.9, 4.0	Room temperature	Ensemble, Ib	[1]
3.49	4	Ensemble, Ib	[28]
3.45	8	Ensemble, Ib	[32]

APPENDIX C: CHARGE-STATE PHOTOLUMINESCENCE DETAILS

1. Photoluminescence-measurement protocol

PL-spectroscopy measurements are performed with a spectrometer and an attached CCD camera (Princeton Instruments PIXIS 100). A half-wave plate tunes the incident-light polarization so that all four N-V orientations are excited equally. To avoid signal-to-noise degradation by modal noise (i.e., speckle) in the multimode fiber delivering light to the spectrometer, the fiber is taped to a speaker head driven by a 200-Hz sinusoidal voltage [77]. Multiple PL measurements are averaged together and normalized by the exposure time. The homogeneity of the commercial diamonds used in this study is characterized by our measuring PL spectra in five different spots in each of a subset of eight diamonds; the PL intensity and extracted N-V charge-state ratios are found to vary by a maximum of 10% across each diamond sample, indicating reasonable homogeneity within each diamond.

2. Huang-Rhys and Debye-Waller factors

A commonly used method to approximate the charge-state efficiency is the Debye-Waller factor $\tilde{S}$, which is defined in terms of the relative weight of the ZPL fluorescence:

$$\tilde{S}_X = -\ln\left(\frac{I_{\mathrm{ZPL},X}}{I_{\mathrm{total},X}}\right), \tag{C1}$$

where $I_{\mathrm{ZPL},X}$ is the integrated fluorescence of the zero-phonon line of N-V charge-state X's PL spectra and $I_{\mathrm{total},X}$ is the total integrated fluorescence of that charge state [1]. In the limit where the ZPL intensities can be measured with sufficient accuracy, the Debye-Waller factor would enable accurate determination of the relative fluorescence ratio of N-V^- and N-V^0 for a given sample. However, the relative fluorescence ratio alone is insufficient to accurately determine the charge-state efficiency, due to different dynamics (lifetimes, absorption cross sections, etc.) of the N-V^- and N-V^0 systems. The Debye-Waller factor can be derived from a theoretical treatment of the electron-phonon coupling for defects in the diamond lattice by approximating the coupling to be linear in the nuclear displacement [78].

Frequently in the literature the Debye-Waller factor is confused with the Huang-Rhys factor. Huang and Rhys [80] defined the Huang-Rhys factor to be the average number of photons of a k-phonon transition emitted in an optical transition [32]. Here the ZPL is weighted with an additional prefactor of the cube of the optical emission frequency, which decreases the Debye-Waller factor compared with the Huang-Rhys factor. To avoid confusion, we follow the naming convention suggested in Ref. [32], denoting the Huang-Rhys factor by S and the Debye-Waller factor by $\tilde{S}$.

During this study, we find determination of the charge-state efficiency using the Debye-Waller decomposition to be nonideal since PL features from other defects can obscure the ZPL, making accurate determination of the Debye-Waller (or Huang-Rhys) factor difficult. This is most problematic for the N-V^- ZPL, which lies within the N-V^0-phonon-sideband emission spectra. Additionally, the ZPL prominence relative to the total PL is small at room temperature for both N-V^- and N-V^0. Because, in part, of both nonidealities, there is substantial variation in the Debye-Waller factors reported in the literature. Measured values of $\tilde{S}$ for N-V^- in the literature are shown in Table II. The Debye-Waller factor for N-V^0 is less studied and is reported to be 3.3 at low temperature [81].

To calculate the fractional contributions of N-V^0 and N-V^- to the total PL using the Debye-Waller factor, we fit and subtract a local linear background to the ZPL of each charge state and fit a Gaussian to the modified ZPL. The ZPL areas $I_{\mathrm{ZPL},0}$ and $I_{\mathrm{ZPL},-}$ for N-V^0 and N-V^-, respectively, are weighted with the Debye-Waller factors reported in Ref. [1]: $\tilde{S}_0 = 3.3$ for N-V^0 and $\tilde{S}_- = 4.3$ for N-V^-. Use of the form of ζ in Eq. (1) with the weighted ZPL areas (normalized by the charge-state PL rate κ_{532}) gives the charge-state efficiency as determined with the Debye-Waller decomposition, ζ^{DW}:

$$\zeta^{\mathrm{DW}} = \frac{I_{\mathrm{ZPL},-}e^{\tilde{S}_-}}{\kappa_{532}I_{\mathrm{ZPL},0}e^{\tilde{S}_0} + I_{\mathrm{ZPL},-}e^{\tilde{S}_-}}. \tag{C2}$$

The Debye-Waller decomposition provides fair performance for diamonds with low N-V^0 fluorescence, which allows easy extraction of the N-V^- ZPL area [1]. However, for diamonds with a high fraction of N-V^0 fluorescence (in this study, diamonds with higher irradiation doses), determining the N-V^- ZPL area becomes difficult. Figure 4 shows the PL ratio (i.e., c_-/c_0) determined with the Debye-Waller decomposition for sample S for various laser excitation intensities. The increasingly large error bars and systematic errors at higher laser intensities reflect the difficulty in determining the N-V^- ZPL area when the N-V^0 photoluminescence dominates. Not only does the basis-function decomposition lead to lower statistical errors in determination of the charge-state fluorescence ratio, but the method is particularly advantageous at the higher laser intensities where the Debye-Waller decomposition becomes unreliable.

3. Construction of basis functions

As the N-V^0 ZPL lies outside the N-V^- PL spectrum, the N-V^- basis function can be created nearly free from N-V^0. The little if any impurity is bounded in two ways and the basis-function shape can be checked itself. First, by comparing peak deviations of the N-V^- basis function around 575 nm, we determine that the N-V^- basis function contains less than 0.015 N-V^0. Second, fitting a Lorentzian in the vicinity of 575 nm with full width at half maximum bounded to lie in the range from 2 to 5 nm suggests at most the N-V^- basis function contains 0.003 N-V^0. Third, the extracted N-V^- basis function is in good agreement with theoretical predictions [28,32,35] derived from experimentally determined single-phonon-sideband spectra from the $^3A_2 \leftrightarrow {}^3E$ transition (see Fig. 1). Given the good fit with theory and the lack of any discernible N-V^0 ZPL in the N-V^- basis functions, we conclude that any contamination of the N-V^- basis function with N-V^0 is on the 1% level or below. Residual fits to the $\hat{I}_0^{\mathrm{pre}}$ function suggest 0.064 ± 0.033 is N-V^-. As this component is removed, we expect the any residual component of N-V^- in the N-V^0 basis function is estimated to occur at the 3% level or less.

Further note that the process for constructing basis functions described in the main text is moderately robust to the choice of initial spectra for $\hat{I}_0^{\mathrm{pre}}(\lambda)$ and $\hat{I}_-^{\mathrm{pre}}(\lambda)$. For example, repeating the basis-function construction process with spectra different from yet comparable to the spectra used in the main text yields a maximum 3% difference in the extracted basis functions and a maximum 3% difference in the PL decomposition results from a subset of eight samples. However, because of the difficulty in fully isolating and removing the N-V^- residual contribution from the N-V^0 basis function, selecting initial spectra with maximal N-V^0 and N-V^- contributions for the $\hat{I}_0^{\mathrm{pre}}(\lambda)$ and $\hat{I}_-^{\mathrm{pre}}(\lambda)$ functions, respectively, is recommended.

4. Secondary determination of κ_{532}

To obtain the total N-V content for the irradiation model [Eq. (9)] or to determine the charge-state efficiency, we need to correct the data for the relative PL rate of N-V^- to N-V^0. In the main text, we find $\kappa_{532} = 2.5 \pm 0.5$ by varying the concentration ratio of N-V^- to N-V^0 using different well-below-saturation 532-nm optical excitation intensities. To independently check the measured value of κ_{532}, we use third-party data, where the concentration ratio of N-V^- to N-V^0 is varied electrically. Specifically, we use the data from Fig. 4(a) in Ref. [23] where a bias voltage is used to vary the concentration ratio of N-V^- to N-V^0. More-positive bias voltages skew the favored charge state toward N-V^0, while more-negative bias voltages skew the favored charge state toward N-V^-.

We denote the PL spectra with 0 V applied as $f'_{\text{N-}V^-}(\lambda)$ and the PL spectra with 35 V applied as $f'_{\text{N-}V^0}(\lambda)$, which correspond to when the diamond studied in Ref. [23] is primarily in the N-V^- and N-V^0 charge states, respectively. These spectra are not area-normalized. From the raw data for Fig. 4(a) in Ref. [23] provided by the authors, we calculate a *preliminary* charge-state PL ratio

$$\kappa'_{532} = \left[\frac{\int_\lambda f'_{\text{N-}V^-}(\lambda)d\lambda}{\int_\lambda f'_{\text{N-}V^0}(\lambda)d\lambda}\right]_{[\text{N-}V^0]=[\text{N-}V^-]}. \tag{C3}$$

This value of κ'_{532} will need to be corrected since the voltage only partially influences the charge state. Straightforward evaluation gives $\kappa'_{532} = 1.687$.

We now describe how κ'_{532} is corrected to obtain the true value of κ_{532}. We desire to obtain the true charge-state PL ratio $\kappa_{532} = \int_\lambda I_-(\lambda)d\lambda / \int_\lambda I_0(\lambda)d\lambda$. We first express the normalized spectra from Fig. 4(a) in Ref. [23] as a linear combination of the normalized basis spectra, $\hat{I}_0(\lambda)$ and $\hat{I}_-(\lambda)$ (see Figs. 1 and 2):

$$\hat{f}'_{\text{N-}V^-}(\lambda) = \alpha\hat{I}_0(\lambda) + (1-\alpha)\hat{I}_-(\lambda), \tag{C4}$$

$$\hat{f}'_{\text{N-}V^0}(\lambda) = (1-\beta)\hat{I}_0(\lambda) + \beta\hat{I}_-(\lambda). \tag{C5}$$

We find $\alpha = 0.0853$ and $\beta = 0.273$. The non-normalized PL spectra can be written as

$$f'_{\text{N-}V^-}(\lambda) = C\left[a_0\hat{I}_0(\lambda) + a_-\kappa_{532}\hat{I}_-(\lambda)\right], \tag{C6}$$

$$f'_{\text{N-}V^0}(\lambda) = C\left[b_0\hat{I}_0(\lambda) + b_-\kappa_{532}\hat{I}_-(\lambda)\right] \tag{C7}$$

where C is an overall scaling constant, and the constants a_0, a_-, b_0, and b_- satisfy

$$a_0 + a_- = b_0 + b_-, \tag{C8}$$

which should be interpreted as the requirement that the sum of the N-V^- and N-V^0 concentrations be independent of the applied voltage. From Eqs. (C6) and (C7) we can rewrite Eq. (C3) as

$$\kappa'_{532} = \frac{a_0 + a_-\kappa_{532}}{b_0 + b_-\kappa_{532}}. \tag{C9}$$

Comparison of Eqs. (C4) and (C5) with Eqs. (C6) and (C7) allows us to note

$$\alpha = \frac{a_0}{a_0 + a_-\kappa_{532}}, \tag{C10}$$

$$\beta = \frac{b_0}{b_0 + b_-\kappa_{532}}. \tag{C11}$$

Solving Eqs. (C8)–(C11) yields $\kappa_{532} = 2.17$. This value of κ should be taken as a lower limit on the true value of κ_{532} at low 532-nm optical excitation intensity since low optical excitation intensity was not used in the work reported in Ref. [23].

APPENDIX D: DETAILS OF THE STUDY OF ANNEALING AND NITROGEN CONVERSION

1. Irradiation studies in the literature

This section reviews prior literature studies reporting monovacancy creation rates by electron irradiation. Figure 10 displays vacancies measured in the diamond literature by UV-vis absorption spectrophotometry for various irradiation doses [11,12,20,26,66,82,85–87], alongside simulated vacancy creation rates from Ref. [84]. In type-IIa diamonds with low concentrations of electron donors, irradiation primarily creates neutral monovacancies (V^0, GR1), whereas in diamonds with a moderate to high concentration of electron donors, such as type-Ib diamonds, negative monovacancies (V^-, ND1) are created at similar or greater rates than neutral monovacancies [11]. Figure 10 depicts only the V^0 concentration for the former sample type and the total vacancy concentration (V^0 plus V^-) for the latter type.

The GR1 center displays a zero-phonon absorption doublet at 740.9 and 744.4 nm [81], while the ND1 center displays a zero-phonon line at 393.6 nm [88]. For the data depicted in Fig. 10, vacancy concentration is calculated by our integrating under the absorption features to obtain A_{GR1} and A_{ND1}, the absorption strengths in meV/cm, and then solving the equations $A_{GR1} = f_{GR1}[V^0]$ and $A_{ND1} = f_{ND1}[V^-]$, where f represents the transition's oscillator strength [9,82]. Davies *et al.* [10] measured the ratio $f_{ND1}/f_{GR1} = 4.0$ using detailed balance arguments applied to an annealing study. Later, Twitchen *et al.* [82] determined that $f_{ND1} = 4.8(2) \times 10^{-16}$ meV cm^2 by correlating ND1 absorption measurements with well-calibrated EPR measurements of V^- concentration. Although V^0 is spinless and thus EPR inactive, f_{GR1} is determined to be $1.2(3) \times 10^{-16}$ meV cm^2 by dividing f_{ND1} by $f_{ND1}/f_{GR1} = 4.0$. These calibration constants were used for all vacancy concentrations reported in Fig. 10.

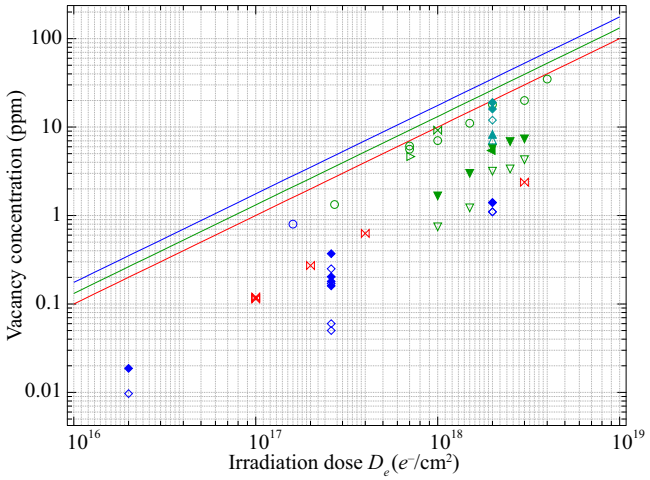

FIG. 10. Reported values of monovacancy concentrations in ppm generated by electron irradiation at 1 MeV (—), 1.9–2 MeV (—), 3 MeV (—), and 4.5–5 MeV (—) from the diamond literature, measured by 77 K UV-Vis spectrophotometry using the oscillator strengths f_{GR1} and f_{ND1} reported in Ref. [82]. Solid lines represent the calculated dependence of vacancy creation on irradiation dose from SRIM calculations [83] in Ref. [84], neglecting vacancy-interstitial recombination for electron irradiation at 1 MeV (—), 2 MeV (—), and 5 MeV (—). Filled markers denote measurements of the total monovacancy concentration $V^0 + V^-$ while open markers denote measurements of only V^0. All diamond samples included here contain nitrogen concentrations $\lesssim 10$ ppm. The following markers denote measurements reported in the following references: ⋈ = this work at 1 MeV, ◀ = Ref. [85] at 1.9 MeV recalculated using f_{GR1} and f_{ND1} from Ref. [82], ▽ and ▼ = Ref. [82] at 1.9 MeV, ⋈ = Ref. [86] at 2 MeV recalculated using f_{GR1} and f_{D1} from Ref. [82], ○ = Ref. [87] at 2 MeV, ▷ = Ref. [20] at 2 MeV, ▲ and △ = Ref. [11] at 3 MeV, ◆ and ◇ = Ref. [12] at 3 MeV, ◆ and ◇ = Ref. [66] at 4.5 MeV, and ○ = Ref. [26] at 4.5 MeV.

Large variation is apparent between data sets from different publications, and, more specifically, between different irradiation facilities. The diamonds in the work reported in Refs. [20,86,87] were all irradiated at Reading University in the United Kingdom and all show significantly higher vacancy creation rates than diamonds irradiated at other facilities. Strikingly, Refs. [87] and [82], published by the same group in the same year using approximately the same electron energy (approximately 2 MeV), report vacancy creation rates of 0.50m cm^{-1} and 1.53 cm^{-1}, respectively, a difference of 3 times. This discrepancy leaves open the possibility of a calibration error

in the applied dosage at one or more irradiation facilities, or a variable that is not controlled for.

Furthermore, although Newton *et al.* [20] observed the vacancy creation rate to be independent of temperature up to 600 K, such temperatures could be exceeded depending on the irradiation setup; inadequate heat sinking combined with a high beam current could cause diamonds to be heated above the temperature at which vacancies become mobile and recombine with interstitial carbon atoms, thereby reducing the measured postirradiation vacancy concentration for a given dose. The diamonds represented in Fig. 10 are irradiated with beam currents ranging from microamperes [82,86,87] to tens of milliamperes [89,90]. In Ref. [66], the vacancies created per dose are seen to vary by more than 2 times between different diamonds. It is unclear whether this variation arises from differences in the samples [10] or inconsistency in the irradiation conditions (such as electron-beam inhomogeneity). It is possible that more than one of these surmised explanations combine to describe the variation depicted in Fig. 10. Moreover, as pointed out in Ref. [8], there is disagreement in the literature on the value of $f_{\mathrm{ND1}}/f_{\mathrm{GR1}}$. In particular, absorption measurements using reversible charge interconversion between GR1 and ND1 find the ratio of oscillator strengths $f_{\mathrm{ND1}}/f_{\mathrm{GR1}}$ to range from 2 to 10 [88,91,92]. This variation suggests a possible uncertainty in the y axis in Fig. 10 of up to approximately 5 times. Such uncertainty complicates the determination of the required irradiation dose to create a fixed vacancy concentration, and thus generate a desired N-V concentration after annealing.

We further note that all measured data points lie below the predicted relationship between dose and vacancy concentration from Ref. [84], in which SRIM calculations were used [83]. These simulations ignore spontaneous recombination, which is crudely estimated to occur 30%–50% of the time for diamonds irradiated with approximately-2-MeV electrons [84,93] and may occur at a higher rate for lower-energy electrons, where the vacancy-interstitial distance is reduced [93]. Uncertainty in the value of $f_{\mathrm{ND1}}/f_{\mathrm{GR1}}$ [13,91] could help account for the discrepancy between the simulations and much of the reported data.

Indirect methods for determining the vacancy concentration produced by a given irradiation dose offer an independent alternative to UV-vis absorption measurements. The indirect method presented in this paper finds a monovacancy creation rate of $B = 0.52 \pm 0.26$ cm^{-1} for 1-MeV electron irradiation by Prism Gem. In comparison, direct vacancy concentration measurements by UV-vis spectroscopy on five similar diamonds irradiated at the same facility (the ⋈ symbols in Fig. 10, excluding the point at 3×10^{18} e^-/cm^2), suggest a V^0 creation rate of 0.30 ± 0.05 cm^{-1} and no production of V^- above the device's V^- detection limit of approximately 100 ppb. The indirect measurements detailed in the main text and these UV-vis measurements are consistent to within the uncertainty in f_{GR1}, which demonstrates the need for additional detailed studies to reduce uncertainty and resolve the aforementioned discrepancies.

2. Diffusion

For one-dimensional diffusion, the rms distance σ from the starting point after N jumps of distance L is given by $\sigma = L\sqrt{N}$. The diffusion coefficient is defined as $D \equiv \sigma^2/(2t_{\mathrm{ann}})$, where t_{ann} is the annealing time during which the diffusion occurs. Combining the two equations allows the diffusion coefficient to be rewritten as $D = L^2\Gamma/2$, where $\Gamma \equiv N/t_{\mathrm{ann}}$ is the vacancy jump frequency. It can be shown that the distance between two adjacent carbon atoms in the diamond lattice is $\frac{a\sqrt{3}}{4}$, where a is the diamond lattice constant. Therefore, in one dimension $L = a/4$. Substitution gives

$$D = \Gamma\frac{a^2}{32}, \tag{D1}$$

which is consistent with alternative derivations [94]. We note that the diffusion constant is independent of the dimensionality, so the diffusion constant above holds for three-dimensional diffusion in the diamond lattice [94].

Comparison of samples with a 1-h postirradiation anneal at 850 °C with samples receiving a 1250 °C postirradiation anneal suggests that the 1250 °C 1-h anneal created approximately 4.5 times as many N-V centers as the 850 °C anneal for an irradiation dose of approximately 10^{16} e^-/cm^2 (see Fig. 5). Under the likely assumption that the 1-h 1250 °C anneal proceeded to completion (no monovacancies are left), this finding suggests that use of only the 1-h 850 °C anneal limits the total N-V concentration to $\chi \approx 1/4.5$ of that expected from the introduced vacancy concentration alone. From the observed value of χ, we can estimate the diffusion constant D as we now describe.

We assume vacancy diffusion can be modeled as a random walk on the diamond lattice and ignore sinks for vacancies other than substitutional nitrogen. We do not correct the data for any time the monovacancy spends in the negative charge state, which is immobile at 850 °C [10,95]. The number of unique lattice sites a vacancy is expected to visit to create a N-V is

$$M_{\mathrm{need}} = \frac{[\mathrm{C}]}{4[\mathrm{N}]F_c}, \tag{D2}$$

where [C] = 1.76×10^{17} cm^{-3} is the density of carbon atoms in diamond and the factor 4 accounts for the four lattice sites adjacent to a substitutional nitrogen, each of which will result in N-V formation if visited by a vacancy.

The number of unique sites visited is

$$M_{\text{visited}} = \Gamma t_{\text{ann}} \eta_{\text{uni}} = 32 D t_{\text{ann}} \eta_{\text{uni}} / a^2, \tag{D3}$$

where η_{uni} characterizes the ratio of unique sites visited to discrete steps during the random walk. Fastenau [96] found the fraction of unique sites visited for a random walk on a diamond lattice to be $n_{\text{uni}} \approx 0.56n + 0.63\sqrt{n}$, where n is the number of steps. This result is similar to the number of distinct sites visited after n steps for other lattices, where for a simple cubic lattice $n_{\text{unique}} \approx 0.66 + 0.57\sqrt{n}$, for a bcc lattice $n_{\text{unique}} \approx 0.72 + 0.52\sqrt{n}$, and for an fcc lattice $n_{\text{unique}} \approx 0.74 + 0.52\sqrt{n}$ [96,97].

We assume the conversion efficiency of the annealing follows

$$\chi = 1 - e^{-M_{\text{visited}}/M_{\text{need}}}. \tag{D4}$$

Combining Eqs. (D2)–(D4) allows the diffusion constant to be written as

$$D = -\frac{[\text{C}] a^2 \log(1-\chi)}{32 t_{\text{ann}} 4[\text{N}] F_c \eta_{\text{uni}}}, \tag{D5}$$

where $\chi \approx 1/4.5$ is the observed annealing efficiency for the 1-h 850 °C anneal. We obtain $D = 1.8\ \text{nm}^2/\text{s}$ for monovacancies at 850 °C, subject to the assumptions of our diffusion model. This value should be compared with the vacancy diffusion constant determined in Ref. [98] ($D = 1.1\ \text{nm}^2/\text{s}$ for annealing at 750 °C) and Ref. [1] (upper limit of $D \leq 40\ \text{nm}^2/\text{s}$ for annealing at 1050 °C).

3. Comparison with crude diffusion theory

A neutral monovacancy in diamond is surrounded by four carbon atoms. The average time for one of the carbon atoms to jump into the vacancy is given by [99]

$$\tau_{\text{carbon}} = \frac{e^{E_a/k_B T}}{\nu_0}, \tag{D6}$$

where $E_a = 2.3 \pm 0.3$ eV [10] is the activation energy, k_B is the Boltzmann constant, T is the temperature, and ν_0 is the attempt frequency for an individual carbon atom. As there are four carbons, the average time for the vacancy to move one lattice site is

$$\tau_{\text{vacancy}} = \frac{e^{E_a/k_B T}}{4\nu_0}, \tag{D7}$$

so we can write the vacancy jumping frequency as

$$\Gamma = 4\nu_0 e^{-E_a/k_B T}. \tag{D8}$$

Plugging the above into Eq. (D1) gives

$$D = \frac{1}{8}\nu_0 a^2 e^{-E_a/k_B T}. \tag{D9}$$

Although the above equation is approximately correct, accurate values of the attempt frequency ν_0 are difficult to determine *a priori* [100]. In particular, Swalin [100] notes, "For want of a suitable value, either the Debye frequency or Einstein frequency can be used but there is no fundamental reason why either is applicable." Nevertheless, use of the diamond Debye frequency of 40 THz for ν_0 results in $D = 30\ \text{nm}^2/\text{s}$, which is much higher than the experimental estimate of $1.8\ \text{nm}^2/\text{s}$. The uncertainty on $E_a = 2.3 \pm 0.3$ results in a roughly 500 times uncertainty in D at 850 °C, so the discrepancy between the experimentally estimated D and that calculated from theory cannot be completely attributed to uncertainty in the value of ν_0.

APPENDIX E: T_2 AND T_1 COHERENCE-STUDY DETAILS

1. T_2-measurement protocol

The T_2 coherence time for each diamond is measured as follows: A moderate magnetic field of 40–60 G is applied along the ⟨111⟩ diamond crystallographic axis, allowing N-V centers of only a single orientation to be addressed. N-V fluorescence collected from a $\pi/2$-π-$\pi/2$ spin-echo sequence and a subsequent $\pi/2$-π-$3\pi/2$ sequence is subtracted and normalized to eliminate common-mode laser-intensity noise and other slow drifts. To avoid anisotropic-hyperfine effects between the N-V spin and the ^{13}C nuclei [74], special care is taken to minimize misalignment of the static magnetic field with the N-V symmetry axis. To achieve this condition, the bias magnetic field is aligned along one of the four diamond crystallographic axes, and only N-V centers parallel to this direction are addressed with resonant microwave radiation. The envelope of the spin-echo signal is modeled as a stretched exponential $e^{-(\tau/T_2)^p}$ with stretched exponential parameter p. While the collapses and revivals in the fluorescence signal due to the ^{13}C nuclei are theoretically described by a fourth-power sinusoid [101] for a single N-V spin, we instead used a linear combination of Lorentzian and Gaussian shapes for each revival to modulate the stretched exponential envelope. The curve fits for our diamonds yield $0.5 < p < 2$. From this fit we extract T_2.

2. T_1-measurement protocol

The longitudinal relaxation time T_1 is measured as follows: N-V centers are first optically initialized into the $m = 0$ state. Thereafter a near-resonant microwave π pulse transfers the population to the $m = 1$ state, after which the population relaxes for a variable time τ toward the thermal-equilibrium mixed state before being read out with a second optical pulse. This yields the fluorescence trace m_1. The N-V ensemble is optically initialized and again allowed to relax to thermal equilibrium with no microwave

pulse, giving fluorescence trace m_0. The population difference $m_0 - m_1$ is fit to an exponential decay with decay time T_1. The subtraction of the signals eliminates common-mode noise from laser fluctuations during the measurement and the common fluorescence from the N-V orientations not addressed by the microwave π pulse.

[1] V. M. Acosta, E. Bauch, E. P. Ledbetter, C. Santori, K.-M. C. Fu, P. E. Barclay, R. G. Beausoleil, H. Linget, J. F. Roch, F. Treussart, S. Chemerisov, W. Gawlik, and D. Budker, Diamonds with a high density of nitrogen-vacancy centers for magnetometry applications, Phys. Rev. B **80**, 115202 (2009).

[2] T. Wolf, P. Neumann, K. Nakamura, H. Sumiya, T. Ohshima, J. Isoya, and J. Wrachtrup, Subpicotesla Diamond Magnetometry, Phys. Rev. X **5**, 041001 (2015).

[3] E. E. Kleinsasser, M. M. Stanfield, J. K. Q. Banks, Z. Zhu, W.-D. Li, V. M. Acosta, H. Watanabe, K. M. Itoh, and K.-M. C. Fu, High density nitrogen-vacancy sensing surface created via He+ ion implantation of ^{12}C diamond, Appl. Phys. Lett. **108**, 202401 (2016).

[4] H. Clevenson, M. E. Trusheim, C. Teale, T. Schroder, D. Braje, and D. Englund, Broadband magnetometry and temperature sensing with a light-trapping diamond waveguide, Nature Phys. **11**, 393 (2015).

[5] J. F. Barry, M. J. Turner, J. M. Schloss, D. R. Glenn, Y. Song, M. D. Lukin, H. Park, and R. L. Walsworth, Optical magnetic detection of single-neuron action potentials using quantum defects in diamond, Proc. Natl. Acad. Sci. **113**, 14133 (2016).

[6] G. Chatzidrosos, A. Wickenbrock, L. Bougas, N. Leefer, T. Wu, K. Jensen, Y. Dumeige, and D. Budker, Miniature Cavity-Enhanced Diamond Magnetometer, Phys. Rev. Appl. **8**, 044019 (2017).

[7] C. B. Hartland, Ph.D. thesis, School University of Warwick, 2014.

[8] A. T. Collins, and I. Kiflawi, The annealing of radiation damage in type Ia diamond, J. Phys.: Condens. Matter **21**, 364209 (2009).

[9] G. Davies, Current problems in diamond: Towards a quantitative understanding, Phys. B: Condens. Matter **273**, 15 (1999).

[10] G. Davies, S. C. Lawson, A. T. Collins, A. Mainwood, and S. J. Sharp, Vacancy-related centers in diamond, Phys. Rev. B **46**, 13157 (1992).

[11] A. T. Collins, and A. Dahwich, The production of vacancies in type Ib diamond, J. Phys.: Condens. Matter **15**, L591 (2003).

[12] K. Iakoubovskii, S. Dannefaer, and A. Stesmans, Evidence for vacancy-interstitial pairs in Ib-type diamond, Phys. Rev. B **71**, 233201 (2005).

[13] A. T. Collins, Optical centres produced in diamond by radiation damage, New Diamond Front. Carbon Technol. **17**, 47 (2007).

[14] J. Choi, S. Choi, G. Kucsko, P. C. Maurer, B. J. Shields, H. Sumiya, S. Onoda, J. Isoya, E. Demler, F. Jelezko, N. Y. Yao, and M. D. Lukin, Depolarization dynamics in a Strongly Interacting Solid-State Spin Ensemble, Phys. Rev. Lett. **118**, 093601 (2017).

[15] H. Zheng, J. Xu, G. Iwata, T. Lenz, J. Michl, B. Yavkin, K. Nakamura, H. Sumiya, T. Ohshima, J. Isoya, J. Wrachtrup, A. Wickenbrock, and D. Budker, Zero-field magnetometry based on nitrogen-vacancy ensembles in diamond, arXiv:1811.11498.

[16] N. Manson, and J. Harrison, Photo-ionization of the nitrogen-vacancy center in diamond, Diam. Relat. Mater. **14**, 1705 (2005).

[17] S. Felton, A. M. Edmonds, M. E. Newton, P. M. Martineau, D. Fisher, and D. J. Twitchen, Electron paramagnetic resonance studies of the neutral nitrogen vacancy in diamond, Phys. Rev. B **77**, 081201 (2008).

[18] S. Felton, B. L. Cann, A. M. Edmonds, S. Liggins, R. J. Cruddace, M. E. Newton, D. Fisher, and J. M. Baker, Electron paramagnetic resonance studies of nitrogen interstitial defects in diamond, J. Phys. Condens. Matter **21**, 364212 (2009).

[19] Y. Mita, Change of absorption spectra in type-I b diamond with heavy neutron irradiation, Phys. Rev. B **53**, 11360 (1996).

[20] M. Newton, B. Campbell, D. Twitchen, J. Baker, and T. Anthony, Recombination-enhanced diffusion of self-interstitial atoms and vacancy–interstitial recombination in diamond, Diam. Relat. Mater. **11**, 618 (2002).

[21] L. Childress, M. V. Gurudev Dutt, J. M. Taylor, A. S. Zibrov, F. Jelezko, J. Wrachtrup, P. R. Hemmer, and M. D. Lukin, Coherent dynamics of coupled electron and nuclear spin qubits in diamond, Science **314**, 281 (2006).

[22] N. Aslam, G. Waldherr, P. Neumann, F. Jelezko, and J. Wrachtrup, Photo-induced ionization dynamics of the nitrogen vacancy defect in diamond investigated by single-shot charge state detection, New J. Phys. **15**, 013064 (2013).

[23] H. Kato, M. Wolfer, C. Schreyvogel, M. Kunzer, W. Müller-Sebert, H. Obloh, S. Yamasaki, and C. Nebel, Tunable light emission from nitrogen-vacancy centers in single crystal diamond PIN diodes, Appl. Phys. Lett. **102**, 151101 (2013).

[24] C. Schreyvogel, M. Wolfer, H. Kato, M. Schreck, and C. E. Nebel, Tuned NV emission by in-plane Al-Schottky junctions on hydrogen terminated diamond, Sci. Rep. **4**, 3634 (2014).

[25] X. Zhu, S. Saito, A. Kemp, K. Kakuyanagi, S.-I. Karimoto, H. Nakano, W. J. Munro, Y. Tokura, M. S. Everitt, K. Nemoto, M. Kasu, N. Mizuochi, and K. Semba, Coherent coupling of a superconducting flux qubit to an electron spin ensemble in diamond, Nature **478**, 221 (2011).

[26] E. Fraczek, V. G. Savitski, M. Dale, B. G. Breeze, P. Diggle, M. Markham, A. Bennett, H. Dhillon, M. E. Newton, and A. J. Kemp, Laser spectroscopy of NV^- and NV^0 colour centres in synthetic diamond, Opt. Mater. Express **7**, 2571 (2017).

[27] D. Gatto Monticone, F. Quercioli, R. Mercatelli, S. Soria, S. Borini, T. Poli, M. Vannoni, E. Vittone, and P. Olivero, Systematic study of defect-related quenching of NV luminescence in diamond with time-correlated single-photon counting spectroscopy, Phys. Rev. B **88**, 155201 (2013).

[28] P. Kehayias, M. W. Doherty, D. English, R. Fischer, A. Jarmola, K. Jensen, N. Leefer, P. Hemmer, N. B. Manson, and

D. Budker, Infrared absorption band and vibronic structure of the nitrogen-vacancy center in diamond, Phys. Rev. B **88**, 165202 (2013).

[29] Y. Doi, T. Makino, H. Kato, D. Takeuchi, M. Ogura, H. Okushi, H. Morishita, T. Tashima, S. Miwa, S. Yamasaki, P. Neumann, J. Wrachtrup, Y. Suzuki, and N. Mizuochi, Deterministic Electrical Charge-State Initialization of Single Nitrogen-Vacancy Center in Diamond, Phys. Rev. X **4**, 011057 (2014).

[30] B. Grotz, M. V. Hauf, M. Dankerl, B. Naydenov, S. Pezzagna, J. Meijer, F. Jelezko, J. Wrachtrup, M. Stutzmann, F. Reinhard, and J. A. Garrido, Charge state manipulation of qubits in diamond, Nat. Commun. **3**, 729 (2012).

[31] N. B. Manson, M. Hedges, M. S. J. Barson, R. Ahlefeldt, M. W. Doherty, H. Abe, T. Ohshima, and M. J. Sellars, NV^{-}–N^{+} pair centre in Ib diamond, New J. Phys. **20**, 113037 (2018).

[32] A. Alkauskas, B. Buckley, D. Awschalom, and C. G. V. de Walle, First-principles theory of the luminescence line shape for the triplet transition in diamond NV centres, New J. Phys. **16**, 073026 (2014).

[33] G. Davies, Vibronic spectra in diamond, J. Phys. C: Solid State Phys. **7**, 3797 (1974).

[34] See Supplemental Material at http://link.aps.org/supplemental/10.1103/PhysRevApplied.12.044003 for unity-area-normalized N-V^{-} and N-V^{0} basis spectra data.

[35] M. L. Goldman, M. W. Doherty, A. Sipahigil, N. Y. Yao, S. D. Bennett, N. B. Manson, A. Kubanek, and M. D. Lukin, State-selective intersystem crossing in nitrogen-vacancy centers, Phys. Rev. B **91**, 165201 (2015).

[36] B. M. Mark Mitchell *et al.*, Engauge digitizer: Extracts data points from images of graphs (2018).

[37] A. M. Edmonds, U. F. S. D'Haenens-Johansson, R. J. Cruddace, M. E. Newton, K.-M. C. Fu, C. Santori, R. G. Beausoleil, D. J. Twitchen, and M. L. Markham, Production of oriented nitrogen-vacancy color centers in synthetic diamond, Phys. Rev. B **86**, 035201 (2012).

[38] J.-P. Tetienne, T. Hingant, L. Rondin, A. Cavaillès, L. Mayer, G. Dantelle, T. Gacoin, J. Wrachtrup, J.-F. Roch, and V. Jacques, Spin relaxometry of single nitrogen-vacancy defects in diamond nanocrystals for magnetic noise sensing, Phys. Rev. B **87**, 235436 (2013).

[39] A. O. Sushkov, N. Chisholm, I. Lovchinsky, M. Kubo, P. K. Lo, S. D. Bennett, D. Hunger, A. Akimov, R. L. Walsworth, H. Park, and M. D. Lukin, All-optical sensing of a single-molecule electron spin, Nano Lett. **14**, 6443 (2014).

[40] L. T. Hall, P. Kehayias, D. A. Simpson, A. Jarmola, A. Stacey, D. Budker, and L. C. L. Hollenberg, Detection of nanoscale electron spin resonance spectra demonstrated using nitrogen-vacancy centre probes in diamond, Nat. Commun. **7**, 10211 (2016).

[41] J. M. Taylor, P. Cappellaro, L. Childress, L. Jiang, D. Budker, P. R. Hemmer, A. Yacoby, R. Walsworth, and M. D. Lukin, High-sensitivity diamond magnetometer with nanoscale resolution, Nat. Phys. **4**, 810 (2008).

[42] L. M. Pham, D. L. Sage, P. L. Stanwix, T. K. Yeung, D. Glenn, A. Trifonov, P. Cappellaro, P. R. Hemmer, M. D. Lukin, H. Park, A. Yacoby, and R. L. Walsworth, Magnetic field imaging with nitrogen-vacancy ensembles, New J. Phys. **13**, 045021 (2011).

[43] M. V. G. Dutt, L. Childress, L. Jiang, E. Togan, J. Maze, F. Jelezko, A. S. Zibrov, P. R. Hemmer, and M. D. Lukin, Quantum register based on individual electronic and nuclear spin qubits in diamond, Science **316**, 1312 (2007).

[44] N. Y. Yao, L. Jiang, A. V. Gorshkov, P. C. Maurer, G. Giedke, J. I. Cirac, and M. D. Lukin, Scalable architecture for a room temperature solid-state quantum information processor, Nat. Commun. **3**, 800 (2012).

[45] H. J. Mamin, M. Kim, M. H. Sherwood, C. T. Rettner, K. Ohno, D. D. Awschalom, and D. Rugar, Nanoscale nuclear magnetic resonance with a nitrogen-vacancy spin sensor, Science **339**, 557 (2013).

[46] S. J. Devience, L. M. Pham, I. Lovchinsky, A. O. Sushkov, N. Bar-Gill, C. Belthangady, F. Casola, M. Corbett, H. Zhang, M. Lukin, H. Park, A. Yacoby, and R. L. Walsworth, Nanoscale NMR spectroscopy and imaging of multiple nuclear species, Nat. Nanotechnol. **10**, 129 (2015).

[47] D. R. Glenn, D. B. Bucher, J. Lee, M. D. Lukin, H. Park, and R. L. Walsworth, High-resolution magnetic resonance spectroscopy using a solid-state spin sensor, Nature **555**, 351 (2018).

[48] P. Kehayias, A. Jarmola, N. Mosavian, I. Fescenko, F. M. Benito, A. Laraoui, J. Smits, L. Bougas, D. Budker, A. Neumann, S. R. J. Brueck, and V. M. Acosta, Solution nuclear magnetic resonance spectroscopy on a nanostructured diamond chip, Nat. Commun. **8**, 188 (2017).

[49] M. Pfender, N. Aslam, H. Sumiya, S. Onoda, P. Neumann, J. Isoya, C. A. Meriles, and J. Wrachtrup, Nonvolatile nuclear spin memory enables sensor-unlimited nanoscale spectroscopy of small spin clusters, Nat. Commun. **8**, 834 (2017).

[50] N. Aslam, M. Pfender, P. Neumann, R. Reuter, A. Zappe, F. Fávaro de Oliveira, A. Denisenko, H. Sumiya, S. Onoda, J. Isoya, and J. Wrachtrup, Nanoscale nuclear magnetic resonance with chemical resolution, Science **357**, 67 (2017).

[51] S. Schmitt, T. Gefen, F. M. Stürner, T. Unden, G. Wolff, C. Müller, J. Scheuer, B. Naydenov, M. Markham, S. Pezzagna, J. Meijer, I. Schwarz, M. Plenio, A. Retzker, L. P. McGuinness, and F. Jelezko, Submillihertz magnetic spectroscopy performed with a nanoscale quantum sensor, Science **356**, 832 (2017).

[52] J. M. Boss, K. Cujia, J. Zopes, and C. L. Degen, Quantum sensing with arbitrary frequency resolution, Science **356**, 837 (2017).

[53] I. Lovchinsky, A. Sushkov, E. Urbach, N. de Leon, S. Choi, K. De Greve, R. Evans, R. Gertner, E. Bersin, and C. Müller *et al.*, Nuclear magnetic resonance detection and spectroscopy of single proteins using quantum logic, Science **351**, 836 (2016).

[54] E. Bauch, C. A. Hart, J. M. Schloss, M. J. Turner, J. F. Barry, P. Kehayias, S. Singh, and R. L. Walsworth, Ultralong Dephasing Times in Solid-State Spin Ensembles via Quantum Control, Phys. Rev. X **8**, 031025 (2018).

[55] E. Bauch, S. Singh, J. Lee, C. A. Hart, J. M. Schloss, M. J. Turner, J. F. Barry, L. Pham, N. Bar-Gill, S. F. Yelin, and R. L. Walsworth, Decoherence of dipolar spin ensembles in diamond, arXiv:1904.08763.

[56] B. A. Myers, A. Ariyaratne, and A. C. B. Jayich, Double-Quantum Spin-Relaxation Limits to Coherence of Near-Surface Nitrogen-Vacancy Centers, Phys. Rev. Lett. **118**, 197201 (2017).

[57] C. P. Slichter, *Principles of Magnetic Resonance*, Springer Series in Solid-State Sciences Vol. 1 (Springer, Berlin, Heidelberg, 1990).

[58] A. Jarmola, V. M. Acosta, K. Jensen, S. Chemerisov, and D. Budker, Temperature- and Magnetic-Field-Dependent Longitudinal Spin Relaxation in Nitrogen-Vacancy Ensembles in Diamond, Phys. Rev. Lett. **108**, 197601 (2012).

[59] T. Yamamoto, T. Umeda, K. Watanabe, S. Onoda, M. L. Markham, D. J. Twitchen, B. Naydenov, L. P. McGuinness, T. Teraji, S. Koizumi, F. Dolde, H. Fedder, J. Honert, J. Wrachtrup, T. Ohshima, F. Jelezko, and J. Isoya, Extending spin coherence times of diamond qubits by high-temperature annealing, Phys. Rev. B. **88**, 075206 (2013).

[60] F. Fávaro de Oliveira, D. Antonov, Y. Wang, P. Neumann, S. A. Momenzadeh, T. Häuermann, A. Pasquarelli, A. Denisenko, and J. Wrachtrup, Tailoring spin defects in diamond by lattice charging, Nat. Commun. **8**, 15409 (2017).

[61] K. Iakoubovskii, and A. Stesmans, Dominant paramagnetic centers in ^{17}O-implanted diamond, Phys. Rev. B **66**, 045406 (2002).

[62] E. Kim, V. M. Acosta, E. Bauch, D. Budker, and P. R. Hemmer, Electron spin resonance shift and line width broadening of nitrogen-vacancy centers in diamond as a function of electron irradiation dose, Appl. Phys. Lett. **101**, 082410 (2012).

[63] J. N. Lomer, and A. M. A. Wild, Electron spin resonance in electron irradiated diamond annealed to high temperatures, Radiat. Eff. **17**, 37 (1973).

[64] M. A. Lobaev, A. M. Gorbachev, S. A. Bogdanov, A. L. Vikharev, D. B. Radishev, V. A. Isaev, V. V. Chernov, and M. N. Drozdov, Influence of CVD diamond growth conditions on nitrogen incorporation, Diam. Relat. Mater. **72**, 1 (2017).

[65] R. Balmer, J. Brandon, S. Clewes, H. Dhillon, J. Dodson, I. Friel, P. Inglis, T. Madgwick, M. Markham, and T. Mollart *et al.*, Chemical vapour deposition synthetic diamond: Materials, technology and applications, J. Phys.: Condens. Matter **21**, 364221 (2009).

[66] D. J. Twitchen, S. L. Geoghegan, and N. Perkins, Method for treating single crystal CVD diamond and product obtained (2010), World Patent WO2010/149775 Al.

[67] F. Fávaro de Oliveira, S. A. Momenzadeh, D. Antonov, J. Scharpf, C. Osterkamp, B. Naydenov, F. Jelezko, A. Denisenko, and J. Wrachtrup, Toward optimized surface δ-Profiles of nitrogen-vacancy centers activated by helium irradiation in diamond, Nano Lett. **16**, 2228 (2016).

[68] L. Robledo, H. Bernien, T. van der Sar, and R. Hanson, Spin dynamics in the optical cycle of single nitrogen-vacancy centres in diamond, New J. Phys. **13**, 025013 (2011).

[69] J.-P. Tetienne, L. Rondin, P. Spinicelli, M. Chipaux, T. Debuisschert, J.-F. Roch, and V. Jacques, Magnetic-field-dependent photodynamics of single NV defects in diamond: An application to qualitative all-optical magnetic imaging, New J. Phys. **14**, 103033 (2012).

[70] A. Gupta, L. Hacquebard, and L. Childress, Efficient signal processing for time-resolved fluorescence detection of nitrogen-vacancy spins in diamond, J. Opt. Soc. Am. B **33**, B28 (2016).

[71] L. T. Hall, J. H. Cole, and L. C. L. Hollenberg, Analytic solutions to the central-spin problem for nitrogen-vacancy centers in diamond, Phys. Rev. B **90**, 075201 (2014).

[72] N. Mizuochi, P. Neumann, F. Rempp, J. Beck, V. Jacques, P. Siyushev, K. Nakamura, D. J. Twitchen, H. Watanabe, S. Yamasaki, F. Jelezko, and J. Wrachtrup, Coherence of single spins coupled to a nuclear spin bath of varying density, Phys. Rev. B **80**, 041201 (2009).

[73] G. Balasubramanian, P. Neumann, D. Twitchen, M. Markham, R. Kolesov, N. Mizuochi, J. Isoya, J. Achard, J. Beck, J. Tissler, V. Jacques, P. R. Hemmer, F. Jelezko, and J. Wrachtrup, Ultralong spin coherence time in isotopically engineered diamond, Nat Mater **8**, 383 (2009).

[74] P. L. Stanwix, L. M. Pham, J. R. Maze, D. Le Sage, T. K. Yeung, P. Cappellaro, P. R. Hemmer, A. Yacoby, M. D. Lukin, and R. L. Walsworth, Coherence of nitrogen-vacancy electronic spin ensembles in diamond, Phys. Rev. B. **82**, 201201 (2010).

[75] A. C. Frangeskou, A. T. M. A. Rahman, L. Gines, S. Mandal, O. A. Williams, P. F. Barker, and G. W. Morley, Pure nanodiamonds for levitated optomechanics in vacuum, New J. Phys. **20**, 043016 (2018).

[76] B. E. A. Saleh, and M. C. Teich, *Fundamentals of Photonics* (John Wiley and Sons, Inc., Hoboken, NJ, 2007), 2nd ed.

[77] J. Baudrand, and G. Walker, Modal noise in high-resolution, fiber-fed spectra: A study and simple cure, Publ. Astron. Soc. Pac. **113**, 851 (2001).

[78] A. A. Maradudin, Theoretical and experimental aspects of the effects of point defects and disorder on the vibrations of crystals 1, Solid State Phys. **18**, 273 (1966).

[79] S. Y. Kilin, A. Nizovtsev, T. Maevskaya, A. Dräbenstedt, and J. Wrachtrup, Spectroscopy on single N–V defect centers in diamond: Tunneling of nitrogen atoms into vacancies and fluorescence spectra, J. Lumin. **86**, 201 (2000).

[80] K. Huang, and A. Rhys, Theory of light absorption and non-radiative transitions in F-centres, Proc. R. Soc. Lond. A. Math. Phys. Sci. **204**, 406 (1950).

[81] A. M. Zaitsev, *Optical Properties of Diamond* (Springer, Berlin, 2001).

[82] D. J. Twitchen, D. C. Hunt, V. Smart, M. E. Newton, and J. M. Baker, Correlation between ND1 optical absorption and the concentration of negative vacancies determined by electron paramagnetic resonance (EPR), Diam. Relat. Mater. **8**, 1572 (1999).

[83] J. F. Ziegler, M. D. Ziegler, and J. P. Biersack, SRIM–the stopping and range of ions in matter, Nucl. Instrum. Methods Phys. Res. Sect. B: Beam Interact. Mater. Atoms **268**, 1818 (2010).

[84] B. Campbell, and A. Mainwood, Radiation damage of diamond by electron and gamma irradiation, Phys. Status Solidi (a) **181**, 99 (2000).
[85] S. C. Lawson, D. Fisher, D. C. Hunt, and M. E. Newton, On the existence of positively charged single-substitutional nitrogen in diamond, J. Phys.: Condens. Matter **10**, 6171 (1998).
[86] L. Allers, A. T. Collins, and J. Hiscock, The annealing of interstitial-related optical centres in type II natural and CVD diamond, Diam. Relat. Mater. **7**, 228 (1998).
[87] D. Twitchen, D. Hunt, M. Newton, J. Baker, T. Anthony, and W. Banholzer, Electron paramagnetic resonance (EPR) and optical absorption studies of defects created in diamond by electron irradiation damage at 100 and 350 K, Phys. B: Condens. Matter **273**, 628 (1999).
[88] H. B. Dyer, and L. du Preez, Irradiation damage in type I diamond, J. Chem. Phys. **42**, 1898 (1965).
[89] Element Six LLC, personal communication (2016).
[90] Prism Gem LLC, personal communication (2016).
[91] K. Iakoubovskii, I. Kiflawi, K. Johnston, A. Collins, G. Davies, and A. Stesmans, Annealing of vacancies and interstitials in diamond, Phys. B: Condens. Matter **340**, 67 (2003).
[92] F. De Weerdt, Ph.D. thesis, School King's College London, University of London, 2007.
[93] G. Davies, B. Campbell, A. Mainwood, M. Newton, M. Watkins, H. Kanda, and T. Anthony, Interstitials, vacancies and impurities in diamond, Phys. Status Solidi (a) **186**, 187 (2001).
[94] P. Pichler, *Intrinsic Point Defects, Impurities, and Their Diffusion in Silicon* (Springer-Verlag Wien, New York, 2004).
[95] S. J. Breuer, and P. R. Briddon, Ab initio investigation of the native defects in diamond and self-diffusion, Phys. Rev. B **51**, 6984 (1995).
[96] R. Fastenau, Ph.D. thesis, School Technische Hogeschool Delft, 1982.
[97] G. H. Vineyard, The number of distinct sites visited in a random walk on a lattice, J. Math. Phys. **4**, 1191 (1963).
[98] J. Martin, R. Wannemacher, J. Teichert, L. Bischoff, and B. Köhler, Generation and detection of fluorescent color centers in diamond with submicron resolution, Appl. Phys. Lett. **75**, 3096 (1999).
[99] R. C. Fletcher, and W. L. Brown, Annealing of bombardment damage in a diamond-type lattice: Theoretical, Phys. Rev. **92**, 585 (1953).
[100] R. A. Swalin, in *Atomic Diffusion in Semiconductors*, edited by D. Shaw (Plenum Press, London and New York, 1973), Chap. 2, p. 65.
[101] A. Laraoui, F. Dolde, C. Burk, F. Reinhard, J. Wrachtrup, and C. Meriles, High-resolution correlation spectroscopy of ^{13}C spins near a nitrogen-vacancy centre in diamond, Nat. Commun. **4**, 1651 (2013).